Thin–Walled Structures 231 (2026) 115485

Contents lists available at ScienceDirect

Thin-Walled Structures

journal homepage: www.elsevier.com/locate/tws

Full length article

Investigation of nonlinear sound transmission caused by geometric large deformation in composite laminated plates

Xiansong Gao [a,b], Xin Fang [a,b,*], Li Cheng [c]

[a] National Key Laboratory of Equipment State Sensing and Smart Support, National University of Defense Technology, Changsha 410073, China
[b] College of Intelligence Science and Technology, National University of Defense Technology, Changsha 410073, China
[c] Department of Mechanical Engineering, The Hong Kong Polytechnic University, Kowloon, Hong Kong, China

ARTICLE INFO

Keywords:
Geometry nonlinearity
Nonlinear sound transmission
Composite laminated plate
Spectral Chebyshev method
Incremental harmonic balance method
Sound insulation

ABSTRACT

Motivated by the knowledge gap on nonlinear sound transmission of acoustically excited structures with large geometric deformations, this paper proposes the Spectral Chebyshev-Incremental Harmonic Balance (SC-IHB) method for analyzing the nonlinear sound transmission properties of a composite laminated plate. The plate generates large deformation vibration subjected to strong sound excitation, modeling in the frame of Von Karman theory and Rayleigh-Ritz principle. It reveals that nonlinearity entails the suppression of structural vibration and significantly increases the sound transmission loss (STL) within the resonance band, due to primary resonance condition. Two specific STL valleys are observed in non-resonance bands, in which vibration is suppressed but total transmitted sound is increased, attributing to the superharmonic resonances enhanced by geometric nonlinear during sound radiation process. The enhancement index just right equals to the superharmonic order. Moreover, geometry nonlinearity also slightly reduces STL in bifurcation band. These properties are confirmed by the time-domain integration method. Therefore, this paper reveals properties of nonlinear sound insulation, and elucidates their harmonic resonance mechanisms. The study deepens the understanding of nonlinear sound transmission of plates, and provides theoretical guidance on the design of high-performance sound proofing structures.

1. Introduction

Plates, the basic components in industries, are commonly subjected to strong noise especially in aircraft and high-speed trains, causing nonlinear large deformation vibration (Fig. 1a). Investigating their nonlinear vibrations and sound transmission characteristics, from the perspective of modelling methods and dynamic mechanisms, is of vital significance for designing plate-based structures.

Nonlinear vibration properties of plates have attracted great attention, including bare plates[1], stiffened plates[2], composite plates[3,4], bistable plates[5,6], and nonlinear metamaterial plates[7,8]. Their nonlinear vibration primarily originates from the stretching effect of their mid-plane induced by large geometrical deformation. By employing Von-Karman theory to describe the nonlinear strain-displacement relationship, typical nonlinear phenomena in plates have been scrutinized, such as nonlinear frequency[9], bifurcation[3], harmonic effects [4], and chaos[3]. Bistable plates show ‘snap-through’ behavior between two stable states, thereby providing novel insights for advancing nonlinear vibration control[5]. Additionally, nonlinear metamaterial plates, embedded with nonlinear oscillators, were shown to entail ultra-low-frequency and ultra-broadband vibration suppression [10,11] while offering enormous room for wave manipulation through chaotic bands and bridging coupling effects[12,13]. These studies have clarified most salient nonlinear vibration phenomena in plates.

Acoustic-structure interaction[14–16] has been a hot topic in recent two decades, including the rise of acoustic/mechanical metamaterials [17–21] for acoustic applications such as sound absorption[22], insulation[23], radiation control[24], or sound wave manipulation[24,25]. Song et al. [23] adopted bandgap control theory to explore the broadband sound insulation of metamaterial plates. Li et al.[26] designed a multifunctional plate to achieve simultaneous sound absorption, insulation, and vibration control. Some studies also showed sound transmission enhancement [27]. However, most existing studies in acoustic-structure interaction are limited to linear dynamics.

* Corresponding author at: National Key Laboratory of Equipment State Sensing and Smart Support, National University of Defense Technology, Changsha 410073, China.

E-mail address: xinfangdr@sina.com (X. Fang).

https://doi.org/10.1016/j.tws.2026.115485
Received 27 February 2026; Received in revised form 30 June 2026; Accepted 3 August 2026
Available online 4 August 2026
0263-8231/

Most studies in nonlinear acoustic-structure interaction in aero-acoustics only consider the flow effects and neglect the structural deformation or vibration [28]. Ginsberg[29,30], Nayfeh[31] and Kelly investigated the formation, evolution, and propagation of shock waves in nonlinear acoustics. Nonlinear acoustic-structure interaction can induce interesting dynamic effects, including harmonics [32], 2:1 internal resonance [33], and nonlinear “lock-in” effects[34]. Zhu et al.[35] optimized the Helmholtz resonators with serrated necks for and improving nonlinear acoustic energy dissipation under high sound excitation. Tang et al.[36] constructed an nonlinear acoustic-solid model of porous honeycomb sandwich plates under high incident sound through experiment and FEM. Nonlinear acoustic metamaterial plates[8] can suppress vibration/acoustic radiation[7] and improve sound insulation[14,37] based on dual-position nonlinear interaction[38]. Therefore, though abroad attentions have been attracted on the nonlinear acoustic-structure problems, research on the nonlinear sound transmission and insulation induced by large deformation plates remains scarce, which motived the present study.

To examine the above issues, an accurate nonlinear acoustic-structure coupling model is fundamentally critical to elucidate nonlinear sound phenomena. Traditional closed-form solutions[39,40] were limited by specific boundary condition assumptions and were inapplicable in nonlinear systems. The time-domain analysis methods (Runge-Kutta, Newmark-β) are less efficient for computing nonlinear amplitude-frequency responses. To tackle the problem, this paper first develops a numerical model for large-deformation plate structures based on the Spectral Chebyshev (SC) method[41,42] within the framework of the First order shear deformation theory (FSDT) and the Von Karman theory. We adopt global basis function expansion (Chebyshev polynomials) to achieve spectral space transformation of the displacement field. Moreover, we develop a nonlinear frequency-domain analysis technique (i.e., the Incremental Harmonic Balance IHB method) for efficient and accurate computation. Then, we investigate the influence of the geometrical nonlinearity on sound transmission as well as the underlying physics governed by bifurcation, superharmonics, and sound radiation modes. Therefore, the paper provides new method and new physics for the sound insulation of plates.

2. Modelling method and algorithm

This section introduces a plate model, theoretical modelling procedure and the corresponding solving algorithm. Owing to its excellent mechanical performances, such as lightweight, high strength, impact resistance, and designability, a plate made of fiber-reinforced laminated composite materials is considered. Exposed to strong sound field at both sides, the plate undergoes large deformation with non-negligeable geometric nonlinearity. The Spectral Chebyshev—Incremental Harmonic Balance (SC-IHB) method is established to solve this sound-plate interaction problem via considering multiple high-order harmonics (Fig. 1b).

As shown in Fig. 1, the rectangular plate, with full clamped boundary, is immersed in a sound field. Incident plane waves (sound) from one side cause wave reflection and plate vibration, which in turn radiates sound to the other side. The composite laminated plate (CLP) consists of N_{ply} layers of fiber-reinforced laminates. The corresponding coordinate system of CLP model are defined by the geometric middle plane. As shown in Fig. 1(c), the distances from the top and bottom surfaces of the k^{-th} layer to the geometric mid-surface are denoted by z_{k+1} and z_k. Five boundary springs k_t ($t = u, v, w, x, y$) are employed to obtain the boundary condition with various stiffness values.

We employ a COMSOL-based time-domain integration model to compute large deformation vibration and the transmitted sound under high-intensity acoustic excitation, as shown in Fig. 2. The large deformation composite laminate plate is created by ‘Layered Material’ option in COMSOL; Transmitted sound field represented by a hemispherical domain accounting for non-planar waves from the plate. Perfectly Matched Layer (PML) is adopted for non-reflective boundary. Mesh configurations for each component are detailed in Fig. 2(b), with mesh sizes satisfying acoustic wavelength resolution requirements to ensure converged results.

Parameters tabulated in Table 1 are used in numerical studies unless otherwise specified. The plate, with length L_x, width L_y and thickness h, is fully clamped (CCCC) at its four edges. $E_1, E_2, \mu_{12}, G_{12}, G_{13}, G_{23}$ are denoted as Young's modulus, Poisson's ratio and shear modulus of composite laminated plate, with stacking sequence [45°/−45°/45°/−45°], referred to Appendix A for details. ρ is the density of plates. θ_{ply} and N_{ply} are the ply angle and ply number of the fiber-reinforce composite material. c_{fluid} is sound speed and ρ_{fluid} is the density of the acoustic medium. PI is incident sound pressure amplitude in decibels (dB). The value for boundary spring stiffness k_t ($t = u, v, w, x, y$) can be determined by Table 2 [41,43].

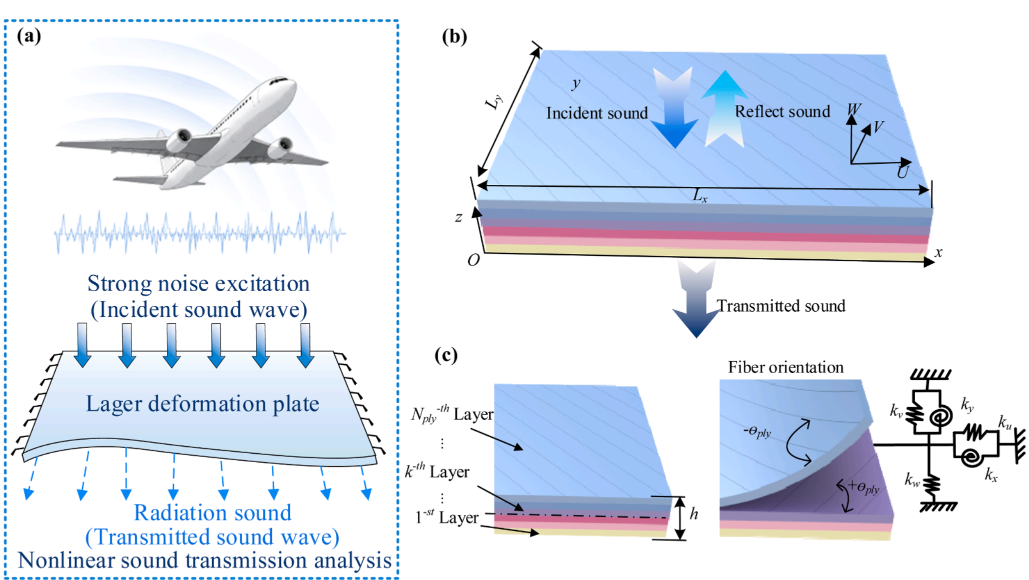

Fig. 1. Model description of composite laminated plate under strong noise environment. (a) The engineering background of this investigation; (b) The theoretical model of nonlinear amplitude-frequency analysis method by SC-IHB method. (c) Lamination, material coordinate system and boundary condition of the CLP.

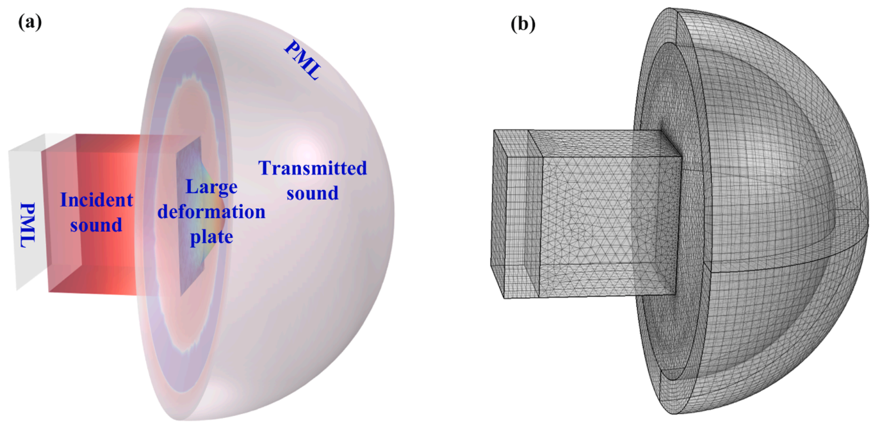

Fig. 2. Time-domain integral model in COMSOL. (a) Time-domain model diagram; (b) Mesh type diagram for each part.

Table 1
Parameters of composite laminated plate under strong noise excitations.

Symbol	Definition	Value	Symbol	Definition	Value
L_x	Length	0.8 m	E_1	Young's	150 GPa
L_y	Width	0.6 m	E_2	Modulus	10 GPa
h	Thickness	2 mm	μ_{12}	Poisson's Ratio	0.25
c_{fluid}	Sound speed	343 m/s	G_{12}	Shear	$0.5E_2$
ρ_{fluid}	Density of air	1.21 kg/m^3	G_{13}	Modulus	$0.5E_2$
PI	Incident sound pressure	140 dB	G_{23}		$0.6E_2$
M	Truncation number of	18	ρ	Density of plate	1500 kg/m^3
N	Chebyshev polynomial	18	θ_{ply}	Ply angle	45°
N_h	Numbers of harmonics term	5	N_{ply}	Number of ply layers	4

Table 2
Parameters of spring stiffness values for various boundary conditions[41].

Boundary Condition (B.C)	Corresponding boundary stiffness value				
	k_u	k_v	k_w	k_x	k_y
F (Free boundary)	0	0	0	0	0
C (clamp boundary)	10^{16}	10^{16}	10^{16}	10^{16}	10^{16}
S (Simply-supported boundary)	10^{16}	10^{16}	10^{16}	0	10^{16}

2.1. Mathematical model of the fiber-reinforced laminated composite materials

This subsection introduces the mathematical model of the fiber-reinforced laminated composite material plates. The composite laminated plate (CLP) is modelled using the First Order Shear Deformation Theory (FSDT)[42,44,45], in which the displacement of any point in the CLP writes:

$$\mathbf{U}=\begin{bmatrix}U(x,y,z,t)\\V(x,y,z,t)\\W(x,y,z,t)\end{bmatrix}=\begin{bmatrix}1 & & & z & \\ & 1 & & & z\\ & & 1 & & \end{bmatrix}\begin{bmatrix}u(x,y,t)\\v(x,y,t)\\w(x,y,t)\\\phi_x(x,y,t)\\\phi_y(x,y,t)\end{bmatrix}=\mathbf{Lu}, \tag{1}$$

where (u, v, w) respectively denote the translational displacement of a point on the middle surface of CLP. ϕ_x and ϕ_y denote the rotational angles along y and x axis on the middle surface, respectively. t is time. According to the Von-Karman large deformation assumption[46,47], the nonlinear strain-displacement relationship writes:

$$\begin{aligned}&\varepsilon_x=\frac{\partial u}{\partial x}+z\frac{\partial \phi_x}{\partial x}+\frac{1}{2}\left(\frac{\partial w}{\partial x}\right)^2;\quad \varepsilon_y=\frac{\partial v}{\partial y}+z\frac{\partial \phi_y}{\partial y}+\frac{1}{2}\left(\frac{\partial w}{\partial y}\right)^2;\\&\gamma_{xy}=\left(\frac{\partial u}{\partial y}+\frac{\partial v}{\partial x}\right)+z\left(\frac{\partial \phi_x}{\partial y}+\frac{\partial \phi_y}{\partial x}\right)+\frac{\partial w}{\partial x}\frac{\partial w}{\partial y};\quad \gamma_{xz}=\frac{\partial w}{\partial x}+\phi_x;\\&\gamma_{yz}=\frac{\partial w}{\partial y}+\phi_y.\end{aligned} \tag{2}$$

According to the generalized Hooke's law [48-50], the stress-strain relationship in the k^{th} layer in the composite plate can be expressed as

$$\begin{Bmatrix}\sigma_x^k\\\sigma_y^k\\\tau_{yz}^k\\\tau_{xz}^k\\\tau_{xy}^k\end{Bmatrix}=\begin{bmatrix}Q_{11}^k & Q_{12}^k & 0 & 0 & 0\\Q_{12}^k & Q_{22}^k & 0 & 0 & 0\\0 & 0 & Q_{44}^k & 0 & 0\\0 & 0 & 0 & Q_{55}^k & 0\\0 & 0 & 0 & 0 & Q_{66}^k\end{bmatrix}\begin{Bmatrix}\varepsilon_x^k\\\varepsilon_y^k\\\gamma_{yz}^k\\\gamma_{xz}^k\\\gamma_{xy}^k\end{Bmatrix}. \tag{3}$$

Here, σ^k, ε^k, Q^k represent stress, strain and elastic stiffness coefficients of the k^{th} layer, respectively. In FSDT, it is assumed that the shear stress σ_z= 0. This simplification is derived from three-dimensional elasticity theory based on engineering requirements (see Abramovich et al.[51], Refer to Appendix A for details).

Therefore, the elastic strain energy (U^{plate}), kinetic energy (T^{plate}) and work (W^{plate}) in CLP can first be obtained as:

$$U^{plate}=\frac{1}{2}\int_0^{L_x}\int_0^{L_y}\left\{\sum_{k=1}^{N_{ply}}\int_{z_k}^{z_{k+1}}\left[\sigma_x^k\varepsilon_x^k+\sigma_y^k\varepsilon_y^k+\kappa_s\tau_{yz}^k\gamma_{yz}^k+\kappa_s\tau_{xz}^k\gamma_{xz}^k+\tau_{xy}^k\gamma_{xy}^k\right]\right\}\mathrm{d}y\mathrm{d}x, \tag{4}$$

$$T^{plate}=\frac{1}{2}\int_0^{L_x}\int_0^{L_y}\left[I_0\left(\dot{u}^2+\dot{v}^2+\dot{w}^2\right)+2I_1\dot{u}\dot{\phi}_x+2I_1\dot{v}\dot{\phi}_y+I_2\left(\dot{\phi}_x^2+\dot{\phi}_y^2\right)\right]\mathrm{d}y\mathrm{d}x, \tag{5}$$

$$W^{plate}=\int_0^{L_x}\int_0^{L_y}p(x,y,z,t)\mathrm{d}y\mathrm{d}x. \tag{6}$$

Here, p is the external sound pressure excitation. κ_s is the shear correction factor, κ_s= 5/6. (I_0, I_1, I_2) denote the inertia terms, written as:

$$I_0=\sum_{k=1}^{N_{ply}}\rho(z_{k+1}-z_k);\quad I_1=\frac{1}{2}\sum_{k=1}^{N_{ply}}\rho\left(z_{k+1}^2-z_k^2\right);\quad I_2=\frac{1}{3}\sum_{k=1}^{N_{ply}}\rho\left(z_{k+1}^3-z_k^3\right). \tag{7}$$

The boundary conditions of the finite plate are determined by the penalty function method[42,44,45] (also called boundary spring method). Three sets of translational springs (k_u, k_v, and k_w) constrain the translational displacement of CLP boundary along the x, y, and z directions. Two sets of torsional springs (k_x and k_y) constrain the rotational degrees. The potential energy stored by these springs is:

$$\begin{aligned}U^{BD} &= \frac{1}{2}\int_0^{L_x}\left[k_{uy0}u^2 + k_{vy0}v^2 + k_{wy0}w^2 + k_{xy0}{\phi_x}^2 + k_{yy0}{\phi_y}^2\right]_{y=0}dx\\ &+\frac{1}{2}\int_0^{L_x}\left[k_{uyL_2}u^2 + k_{vyL_2}v^2 + k_{uyL_2}w^2 + k_{xyL_2}{\phi_x}^2 + k_{yyL_2}{\phi_y}^2\right]_{y=L_y}dx\\ &+\frac{1}{2}\int_0^{L_y}\left[k_{ux0}u^2 + k_{vx0}v^2 + k_{ux0}w^2 + k_{xx0}{\phi_x}^2 + k_{yx0}{\phi_y}^2\right]_{x=0}dy\\ &+\frac{1}{2}\int_0^{L_y}\left[k_{uxL_1}u^2 + k_{vxL_1}v^2 + k_{wxL_1}w^2 + k_{xxL_1}{\phi_x}^2 + k_{yxL_1}{\phi_y}^2\right]_{x=L_x}dy.\end{aligned} \tag{8}$$

Thus, the overall Lagrange energy generalization for CLP can be written as:

$$L = U^{plate} + W^{plate} - T^{plate} + U^{BD}. \tag{9}$$

2.2. 2.2 Spectral Chebyshev (SC) method for displacement solution

This subsection employs the Spectral Method to perform spectral expansion of the displacement field. Common orthogonal polynomials for expansion include characteristic orthogonal polynomials[52], Chebyshev polynomials[53,54], Legendre polynomials[41,42], and improved Fourier series[55]. Among those, Chebyshev polynomials exhibit numerical stability and accuracy. Therefore, the displacement field $\mathbf{u}$ is converted to spectral space using Chebyshev polynomials, i.e., the Spectral Chebyshev (SC) method, which is expressed as:

$$\mathbf{u} = diag(\boldsymbol{\Gamma}_\mathbf{A}, \boldsymbol{\Gamma}_\mathbf{B}, \boldsymbol{\Gamma}_\mathbf{C}, \boldsymbol{\Gamma}_\mathbf{D}, \boldsymbol{\Gamma}_\mathbf{E})\mathbf{q}(t). \tag{10}$$

Here, $\boldsymbol{\Gamma}$ represents the row vector formed by the finite-term Chebyshev polynomials. $\mathbf{q}(t)$= [$\mathbf{A}(t)$; $\mathbf{B}(t)$; $\mathbf{C}(t)$; $\mathbf{D}(t)$; $\mathbf{E}(t)$] is the unknown column vector denoting generalized displacement coefficients. The specific vector forms are in Appendix B. Then, substituting Eq. (10) into Eq. (9) yields the other expression of the Lagrange energy function.

Based on the Rayleigh-Ritz approach[56], the dynamic model for CLP can be derived by performing the extreme value procedure of the partial derivatives for vector $\mathbf{q}$.

$$\begin{gathered}\frac{\partial L}{\partial \mathbf{q}(t)} = 0,\\ \frac{d}{dt}\left(\frac{\partial T^{plate}}{\partial \dot{\mathbf{q}}(t)}\right) - \frac{\partial\left(T^{plate}\right)}{\partial \mathbf{q}} + \frac{\partial\left(U^{plate} + U^{BD}\right)}{\partial \mathbf{q}} = p.\end{gathered} \tag{11}$$

The equations of motion for CLP considering large geometric deformations can then be expressed as

$$\mathbf{M}\ddot{\mathbf{q}}(t) + \mathbf{C}\dot{\mathbf{q}}(t) + [\mathbf{K}_\mathbf{L} + \mathbf{K}_\mathbf{NL}(\mathbf{q}(t))]\mathbf{q}(t) = \mathbf{F}\cos\omega t, \tag{12}$$

where $\mathbf{M}$, $\mathbf{C}$, $\mathbf{K}$ and $\mathbf{K}_\mathbf{NL}$ are respectively the mass, damping, linear stiffness, and nonlinear stiffness matrices, respectively; $\mathbf{F}$ is the force/pressure vector; ω denotes angular frequency. The elements in $\mathbf{M}$, $\mathbf{C}$, $\mathbf{K}$, $\mathbf{K}_\mathbf{NL}$, and $\mathbf{F}$ are listed in Appendix B.

As the composite plate is a high-dimensional nonlinear system, it is necessary to reduce the computational cost through reducing the dimensionality (refer to ref. [57] for dimensionality reduction method). Firstly, by neglecting the damping terms, nonlinear terms, and external load terms in Eq. (12), the degenerated linear free vibration equation of the CLP is obtained as:

$$\left(\mathbf{K}_\mathbf{L} - \omega^2\mathbf{M}\right)\mathbf{q} = \mathbf{0}. \tag{13}$$

By solving the eigenvalue/eigenvector of Eq. (13), the modal matrix $\boldsymbol{\Phi}$ and modal coordinates $\boldsymbol{\zeta}$ can be obtained by representing the displacement vector $\mathbf{q}$ in the following form:

$$\mathbf{q}(t) = \boldsymbol{\Phi}\boldsymbol{\zeta}(t). \tag{14}$$

Here, the first 100 orders are selected as the truncated approximation to represent the displacement. Substituting Eq. (14) into the high-dimensional nonlinear system Eq. (12) gives the following reduced-order form:

$$\begin{gathered}\mathbf{m}\ddot{\boldsymbol{\zeta}}(t) + \mathbf{c}\dot{\boldsymbol{\zeta}}(t) + (\mathbf{k} + \mathbf{k}_{nl})\boldsymbol{\zeta}(t) = \mathbf{f}\cos\omega t,\\ \mathbf{m} = \boldsymbol{\Phi}^T\mathbf{M}\boldsymbol{\Phi};\quad \mathbf{c} = \boldsymbol{\Phi}^T\mathbf{C}\boldsymbol{\Phi};\quad \mathbf{k} = \boldsymbol{\Phi}^T\mathbf{K}\boldsymbol{\Phi};\quad \mathbf{k}_{nl} = \boldsymbol{\Phi}^T\mathbf{K}_n\boldsymbol{\Phi};\quad \mathbf{f} = \boldsymbol{\Phi}^T\mathbf{F}.\end{gathered} \tag{15}$$

2.3. Incremental Harmonic Balance (IHB) method for solutions

This subsection mainly proposes the IHB method for finding the nonlinear solutions. Eq. (15) can be directly solved using time-domain integration methods (such as Newmark-β method, Runge-Kutta method) at a high computational cost. Including the Runge-Kutta method (Ode15s in MATLAB), we further incorporate the Incremental Harmonic Balance (IHB) method [57,58] to acquire steady-state solutions.

Introducing the dimensionless time scale parameter $\tau = \omega t$, the nonlinear dynamic ordinary differential equations of Eq. (15) are casted into the following form:

$$\omega^2\mathbf{m}\ddot{\boldsymbol{\zeta}}(\tau) + \omega\mathbf{c}\dot{\boldsymbol{\zeta}}(\tau) + (\mathbf{k} + \mathbf{k}_{nl})\boldsymbol{\zeta}(\tau) = \mathbf{f}\cos\tau. \tag{16}$$

The first step of the IHB method is the incremental process, which involves linearizing the differential equations using the Newton-Raphson method. Assuming the steady response and excitation parameters at a certain vibration state as $\zeta_{j,0}$, $f_{j,0}$ and ω_0, the adjacent vibration state can be represented by adding corresponding small increments ($\Delta\zeta_j$, Δf_j, and $\Delta\omega$) from them, as follows:

$$\zeta_j = \zeta_{j,0} + \Delta\zeta_j;\quad f_j = f_{j,0} + \Delta f_j;\quad \omega = \omega_0 + \Delta\omega. \tag{17}$$

Here, the subscript j denotes the j-th element in the matrix $\boldsymbol{\zeta}$ and $\mathbf{f}$ of Eq. (16). The vector $\boldsymbol{\zeta}$ and $\mathbf{f}$ can be rewritten as:

$$\boldsymbol{\zeta} = \boldsymbol{\zeta}_0 + \Delta\boldsymbol{\zeta};\quad \mathbf{f} = \mathbf{f}_0 + \Delta\mathbf{f};\quad \omega = \omega_0 + \Delta\omega. \tag{18}$$

By substituting Eq. (18) into Eq. (16) and neglecting the higher-order infinitesimal terms of the increments, the linearized incremental equation of this nonlinear equation is obtained as follows:

$$\begin{gathered}\omega_0^2\mathbf{m}\Delta\ddot{\boldsymbol{\zeta}} + \omega_0\mathbf{c}\Delta\dot{\boldsymbol{\zeta}} + \left(\mathbf{k} + \frac{\partial\mathbf{k}_{nl}\boldsymbol{\zeta}_0}{\partial\boldsymbol{\zeta}_0}\right)\Delta\boldsymbol{\zeta} = \mathbf{Re} - (2\omega_0\mathbf{m}\ddot{\boldsymbol{\zeta}}_0 + \mathbf{c}\dot{\boldsymbol{\zeta}}_0)\Delta\omega + \Delta\mathbf{f}\cos(\tau),\\ \mathbf{Re} = \mathbf{f}_0\cos(\tau) - \left[\omega_0^2\mathbf{m}\ddot{\boldsymbol{\zeta}}_0 + \omega_0\mathbf{c}\dot{\boldsymbol{\zeta}}_0 + (\mathbf{k} + \mathbf{k}_{nl})\boldsymbol{\zeta}_0\right],\end{gathered} \tag{19}$$

where $\mathbf{Re}$ represents the residual vector, meaning that the numerical solution of the nonlinear system equals the exact solution when $\mathbf{Re} = \mathbf{0}$. $\boldsymbol{\zeta}_0$, $\Delta\boldsymbol{\zeta}$, $\mathbf{f}_0$, and $\Delta\mathbf{f}$ are detailed in Appendix C.

After this step, the harmonic balance procedure is used. The steady-state solution and increments for j-th element of the nonlinear dynamic equations can be expressed in Eq. (20) by employing a finite-term Fourier series (i.e. the expansion of high-order superharmonics in this paper) as:

$$\begin{aligned}\zeta_{j,0} &= a_{j,0} + \sum_{k=1}^{N_h} a_{j,k}\cos k\tau + \sum_{k=1}^{N_h} b_{j,k}\sin k\tau = \mathbf{C}_s\mathbf{A}_j,\\ \Delta\zeta_{j,0} &= \Delta a_{j0} + \sum_{k=1}^{N_h}\Delta a_{j,k}\cos k\tau + \sum_{k=1}^{N_h}\Delta b_{j,k}\sin k\tau = \mathbf{C}_s\Delta\mathbf{A}_j,\end{aligned} \tag{20}$$

where N_h is the number of harmonic terms. $\mathbf{C}_s$, $\mathbf{A}_j$, and $\Delta\mathbf{A}_j$ are detailed in Appendix C.

Finally, the displacement w at point (x_0, y_0) is:

$$w(x_0, y_0, t) = \left[w_{a,0}, w_{a,1}, w_{b,1}, w_{a,2}, w_{b,2}, w_{a,3}, w_{b,3}, \ldots w_{a,Nh}, w_{a,Nh}\right]. \tag{21}$$

Here, column elements of w represent each order harmonic component of displacement. Therefore, the fundamental, i-th order and total harmonic of displacement/velocity can be written as:

$$w_1 = \sqrt{w_{a,1}^2 + w_{b,1}^2};\quad \dot{w}_1 = \sqrt{w_{a,1}^2 + w_{b,1}^2}\cdot\omega;$$
$$w_i = \sqrt{w_{a,i}^2 + w_{b,i}^2};\quad \dot{w}_i = \sqrt{w_{a,i}^2 + w_{b,i}^2}\cdot i\cdot\omega.$$
$$w_{total} = \sqrt{w_{a,0}^2 + \sum_{i=1}^{N_h}\left(w_{a,i}^2 + w_{b,i}^2\right)};\quad \dot{w}_{total} = \sqrt{\sum_{i=1}^{N_h}\left((w_{a,i}\cdot i\cdot\omega)^2 + (w_{b,i}\cdot i\cdot\omega)^2\right)}. \tag{22}$$

Here, w and $\dot{w}$ denote displacement and velocity, respectively. Subscripts ‘1′, ‘i’ and ‘total’ denote the fundamental, i-th order and total harmonic.

2.4. Vibro-acoustic coupling model for sound transmission

This subsection introduces the vibro-acoustic coupling model. The sound wave p applied on the large deformation plate writes:

$$p(x,y,z,t) = p_{inci} + p_{rec} - p_{tra}. \tag{23}$$

Here, p_{inci}, p_{rec} and p_{tra} are the sound pressures of incident, reflected, and transmitted waves. This paper adopts the method described in Ref. [59,60] for modeling the vibro-acoustic problem, i.e., considering the incident wave, reflected wave, and transmitted wave as the sum of blocked pressure and reradiated pressure, and making the transmitted sound wave only related to plates vibration. The pressure sound wave p is rewritten as:

$$p(x,y,z,t) = 2p_{inci}, \tag{24}$$

$$p_{inci}(x,y,z,t) = P_{inci}\cos(k_x x + k_y y + k_z z - \omega t)\big|_{z=0}, \tag{25}$$

$$k_x = k_{fluid}\sin\varphi_{el}\cos\varphi_{az};\quad k_y = k_{fluid}\sin\varphi_{el}\sin\varphi_{az};\quad k_z = k_{fluid}\cos\varphi_{el};\quad k_{fluid} = \omega/c_{fluid}. \tag{26}$$

Here, P_{inci} is the incident sound pressure amplitude. k_{fluid} is wave number. k_x, k_y, and k_z are the components of wave number k_{fluid} in the x, y and z directions. c_{fluid} is sound speed. Besides, the incident elevation angle is φ_{el} and azimuth angle is φ_{az}. This study does not consider the oblique incidence scenarios, i.e., we specify φ_{el}= 0 and φ_{az}= 0.

The transmitted sound can be calculated via Rayleigh integral by taking the normal vibration velocity $\dot{w}$ of the plate as the sound source, which writes [60]:

$$p(\mathbf{d}) = \frac{\mathrm{j}\omega\rho_{fluid}}{2\pi}\int_S \dot{w}(\mathbf{d}_s)\frac{e^{-\mathrm{j}k_{fluid}|\mathbf{d}-\mathbf{d}_s|}}{|\mathbf{d}-\mathbf{d}_s|}\mathrm{d}S. \tag{27}$$

Here, $|\mathbf{d} - \mathbf{d}_s|$ is the distance from $\mathbf{d}_s$ (source point) to $\mathbf{d}$ (field point); ρ_{fluid} is the density of the acoustic medium. As calculating the sound power will encounter the problem of complex quadratic integration, this paper adopts the elementary method instead. The plate is first divided into R = $M_u\times N_u$ computational elements. The vibration of these subunits is determined by the velocity at the center of the element. Therefore, the vibration velocity and sound pressure can then be written in matrix form based on the velocities of these elements as

$$\widetilde{\mathbf{p}}_e = \mathbb{Z}\dot{\mathbf{w}}_e,\quad \dot{\mathbf{w}}_e = [\dot{w}_{e1}, \dot{w}_{e2}, \ldots, \dot{w}_{eR}]^T;\quad \widetilde{\mathbf{p}}_e = [p_{e1}, p_{e2}, \ldots, p_{eR}]. \tag{28}$$

Where $\mathbb{Z}$ is the impedance matrix, whose internal matrix elements are:

$$(\mathbb{Z})_{ij} = \frac{\mathrm{j}\omega\rho_{fluid}S_u}{2\pi}\frac{\mathrm{e}^{-\mathrm{j}k_{fluid}d_{ij}}}{d_{ij}}. \tag{29}$$

Here, d_{ij} represents the distance from the i-th field point to the center of the j-th elemental radiator. S_u represents the area of elemental radiator.

Similarly, sound power $\hat{W}$ can be discretized as:

$$\widehat{W} = \frac{S_u}{2}\mathrm{Re}\left(\dot{\mathbf{w}}_e^H\mathbf{p}_e\right) = \frac{S_u}{2}\mathrm{Re}\left(\dot{\mathbf{w}}_e^H\mathbb{Z}\dot{\mathbf{w}}_e\right) = \dot{\mathbf{w}}_e^H\mathbf{R_a}\dot{\mathbf{w}}_e, \tag{30}$$

in which $\mathbf{R_a}$ denotes the radiation resistance matrix, written as:

$$\mathbf{R_a} = \frac{\omega^2\rho_{fluid}S_u^2}{4\pi c_{fluid}}\widetilde{\mathbf{R}}_{ij};\quad \widetilde{\mathbf{R}}_{ij}\begin{cases}\sin(k_{fluid}d_{ij})/k_{fluid}d_{ij}, i\neq j\\ 1, i=j\end{cases}. \tag{31}$$

The sound pressure level is defined as

$$\mathrm{PI} = 20\log_{10}\left(p_{inci}/p_{ref}\right)\quad (\mathrm{dB}), \tag{32}$$

with $p_{ref} = 2\times10^{-5}$ Pa. Sound power level (SWL), Sound pressure level (SPL) and Sound Radiation Efficiency (SRE) can be expressed as[60]:

$$SWL = 10\log\left(\frac{\widehat{W}}{\widehat{W}_{\mathrm{ref}}}\right);\quad SPL = 20\log\left(\frac{p}{p_{ref}}\right);\quad SRE = \frac{\dot{\mathbf{w}}_e^H\mathbf{R_a}\dot{\mathbf{w}}_e}{\rho_{fluid}c_{fluid}S_u\dot{\mathbf{w}}_e^H\mathbf{N_I}\dot{\mathbf{w}}_e}, \tag{33}$$

in which $\hat{W}_{ref} = 1\times10^{-12}$ W. $\mathbf{N_I}$ denotes the identity matrix.

The incident sound intensity (I_{ic}), incident sound power (W_{ic}) and sound transmission loss (STL) take the following forms, respectively.

$$I_{ic} = \frac{p_{inci}^2\cos\varphi_{el}}{2\rho_{fluid}c_{fluid}};\quad \widehat{W}_{ic} = \frac{p_{inci}^2 L_x L_y\cos\varphi_{el}}{2\rho_{fluid}c_{fluid}};\quad STL = 10\log_{10}(\widehat{W}_{ic}/\widehat{W}). \tag{34}$$

2.5. Validation of the SC-IHB method

This subsection first verifies the SC-IHB method through comparison with results reported in the literature, including vibro-acoustic coupling results in Fig. 3 and nonlinear bifurcation computation in Fig. 4.

Fig. 3 compares vibro-acoustic results calculated by present SC method with those reported in literature (Zhou K et al.[61], Chandra et al.[60], and Geng et al.[62]). Zhou K et al.'s results are numerical solutions based on improved Fourier series. Chandra and Geng’s results can be regarded as exact solutions because the displacements are Levy-Navier type closed-form solutions under simply-support boundary. Fig. 3 clearly shows that the acoustic-vibration coupling model using SC-IHB established in this paper has excellent computational accuracy.

We continue verify the nonlinear amplitude-frequency bifurcation solutions under different loads F and damping coefficient β, shown in Fig. 4. Compared to the results using the perturbation method (by F.B. [63]) and the shooting method (by Ribeiro [64]), the results employing the current SC-IHB method exhibit excellent agreement.

We clarify the influence of block-pressure method in Eq. (24), which neglects the acoustic radiation pressure in dynamic equation. This influence is considered negligible due to its light fluid loading case (i.e., air), causing the plate's impedance approaching the rigid boundary[65]. Roussos [59] and Chandra [60] had demonstrated the validity for calculating plate’s STL in air. Then, we further analyze the influence of the acoustic radiation pressure on the nonlinear large-deformation plate. As illustrated in Fig. 5(a), we build the fully coupled model considering the transmitted pressure and comparative model deleting transmitted field. The results in Fig. 5(b~d) validate the hypothesis of blocked-pressure method to establish the vibro-acoustic coupling model, due to agreement between the two models in time-domain, frequency-domain, and phase portraits.

3. Properties of nonlinear vibro-acoustic responses

This section primarily investigates nonlinear vibrations and associated nonlinear sound transmission caused by geometric deformations in

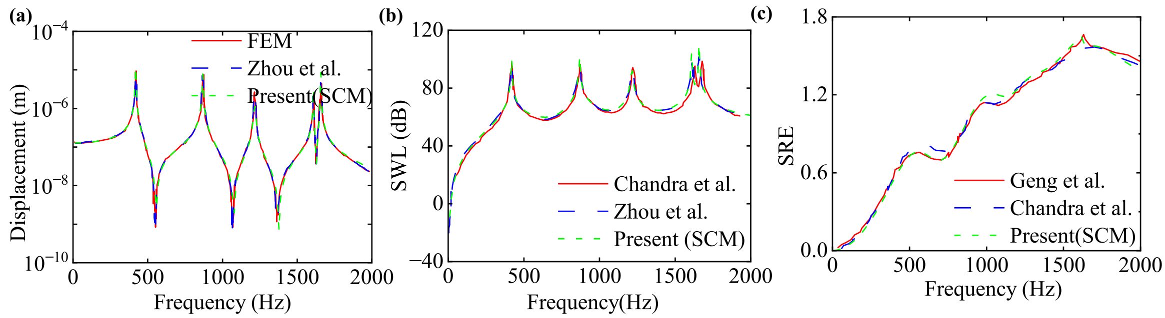

Fig. 3. Verification of vibro-acoustic coupling results calculated by SC-IHB method with Ref.[60–62]: (a) vibration responses; (b) sound power level SWL; (c) sound radiation efficiency SRE.

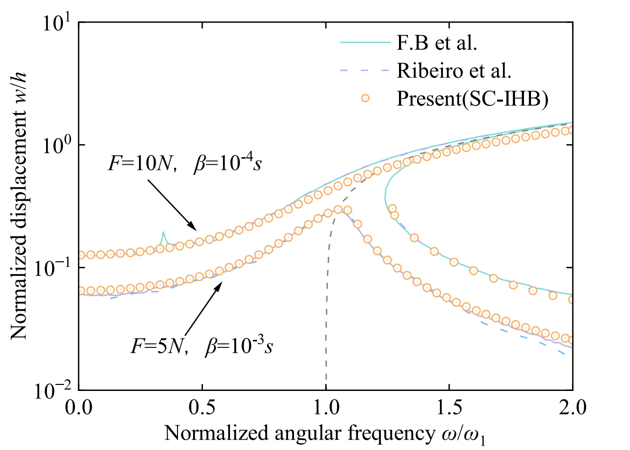

Fig. 4. Computed nonlinear amplitude-frequency bifurcation solutions by current SC-IHB method in comparison with Ref. [63,64]. w/h and ω/ω_1 denote the normalized displacement response and normalized angular frequency around the first resonance frequency, respectively.

plate subjected to strong incident sound. The average vibration transmission on the plate is quantified by

$$H_{vib,av} = 20\log_{10}(\dot{w}_{av}/P_{inci}). \tag{35}$$

Here, $\dot{w}_{av}$ denotes the average vibration velocity of plate, which includes all harmonics. P_{inci} denotes the pressure of the incident sound waves.

Linear problems are first investigated before delving into the nonlinear vibro-acoustic system. Fig. 6 and Fig. 7 present the modal shapes, natural frequencies, and response for the clamp linear plate. The STL curve exhibits obvious valleys caused by modal resonance of the clamp plate under acoustic excitation, including the 1st (43 Hz), 4th (119.64 Hz), 6th (176.22 Hz), 10th (253.03 Hz), 12th (279.3 Hz), and 19th (411.75 Hz) modes. Those mode shapes can be excited by plane sound pressure, while the others cannot due to the normal incidence nature. Moreover, only those mentioned modes can radiate the transmitted sound according to the radiation cancellation principle by Fahy [65]. Besides, those STL valleys are caused by modal resonance in Fig. 6 (b), particularly the 1st resonance frequency named as f_{res1} in this paper.

3.1. Typical bifurcation analyses

We clarify f_0 and f_{res1} denote excitation frequency and 1st nature resonance frequency of the composite laminated plate.

As f_{res1} (43 Hz) in Fig. 6(b) is clearly the frequency where the most intense vibration and the poorest sound insulation performance occur. Therefore, this subsection focuses on analyzing the nonlinear bifurcation characteristics near f_{res1}, as shown in Fig. 8. We distinguish the properties in three frequency ranges: resonance band, non-resonance band, and bifurcation band.

Within resonance band, $H_{vib,av}$ is lower than its counterpart in the linear result, and STL is much higher. This indicates that geometric nonlinearity can elevate sound insulation near f_{res1}. Besides, amplitude-dependent curves of $H_{vib,av}$ and STL exhibit the bifurcation properties of hardening-stiffness nonlinear systems. In the resonance band, the greater incident sound pressure provides higher sound insulation performance. There are three branches after the bifurcation point. The branch−1 and branch−2, denoting the stable solution by solid-line, are shown in Fig. 8 for clarity. And the branch−3 is unstable solution, depicted as dash-line. The arrow indicates the bifurcation point and the unstable state, meaning the nonlinear STL response jumping from stable branch−1 to stable branch−2. The larger incident sound, the higher frequency the point shifts toward. In this range, nonlinearity reduces the STL as compared with the linear results.

We take the responses under 135 dB as an example to investigate the harmonic components, as displayed in Fig. 8(c). Within the resonance band and bifurcation band, the fundamental harmonic remains the dominant component of STL. Interestingly, there are two valleys, marked by blue circles, along the STL curve in the low-frequency region (the stiffness-dominated region). Here, nonlinearity suppresses vibration but enhances transmitted sound, thereby compromising the sound insulation performance. Those frequency areas are closed to 9 Hz and 15 Hz, which correspond to about $f_{res1}/5$ and $f_{res1}/3$, i.e. $f_0 \approx f_{res1}/5$ and $f_0 \approx f_{res1}/3$, exhibiting a distinct superharmonic resonance. Moreover, from the analysis on harmonic components in Fig. 8(c), the valley near 9 Hz is dominated by the 5th harmonic while the valley near 15 Hz by the 3rd harmonic.

We further investigate the bifurcation behavior of the STL under different stacking sequences. as shown in Fig. 9. Although CLP depend strongly on stacking sequence and anisotropic stiffness distribution, similar STL are also observed for different stacking schemes, including [30°/−30°/30°/−30°] and [0°/90°/0°/90°], demonstrating the robustness and generality of the reported nonlinear sound transmission phenomena. Different stacking sequence affects the 1st frequency by anisotropic stiffness distribution, 39 Hz for [30°/−30°/30°/−30°] and 45.5 Hz for [0°/90°/0°/90°], and consequently influence the blue STL valley (blue cycle) and the frequency bifurcation point (arrow).

3.2. Superharmonic enhancement of transmitted sound

This subsection further analyzes the time-domain responses based on finite element simulation in COMSOL to demonstrate the nonlinear sound transmission properties discovered in Fig. 8. We take the incident frequencies of 15 Hz (in non-resonance band), 40 Hz (in resonance band), and 70 Hz (in bifurcation band) as examples to clarify the phenomena. To characterize the interaction between different harmonics, we define energy pumping transfer indices T and superharmonic enhancement index S_{vp} as [7]:

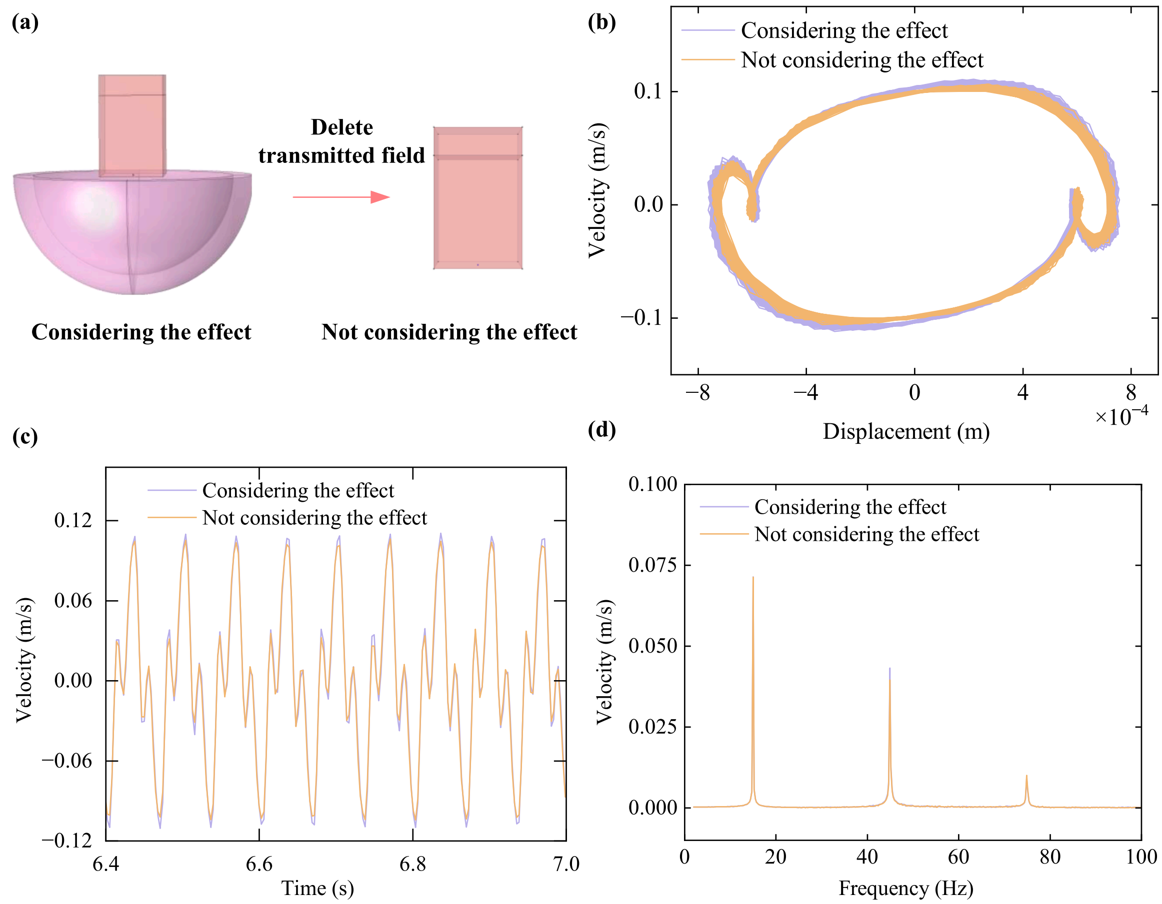

Fig. 5. Analysis the effects of transmitted sound on nonlinear large-deformation plate. (a) Two comparative models. (b~d) Comparison of nonlinear dynamic characteristics of large-deformation plate with and without considering the transmitted sound: (b) phase portraits; (c) Average velocity in time-domain; (d) FFT spectral components of (c).

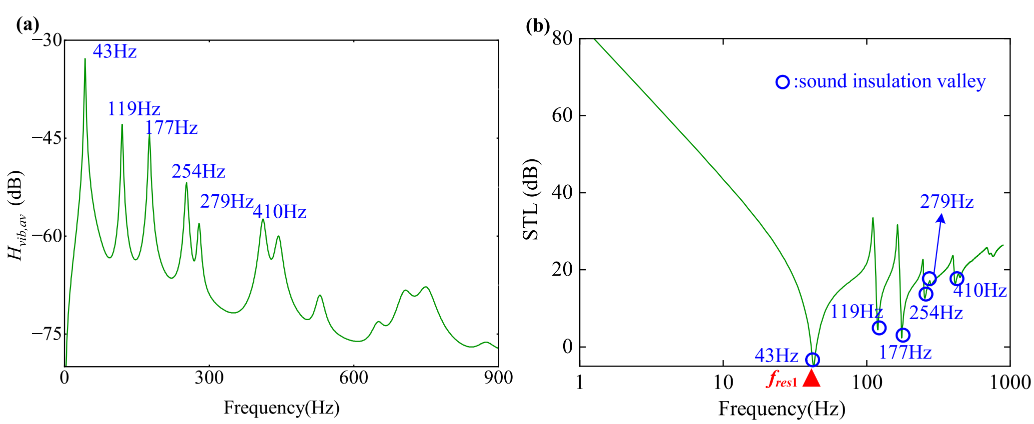

Fig. 6. The linear vibration and sound responses for the clamp plate modelling by SC-IHB method. (a) average vibration transmission $H_{vib,av}$; (b) Linear STL. The red triangle star indicates the 1st resonance frequency f_{res1} for sound insulation valley.

$$T_{v,i} = \frac{\dot{w}_i}{\dot{w}_1}, \quad T_{p,i} = \frac{p_i}{p_1}, \quad S_{vp,i} = \frac{T_{p,i}}{T_{v,i}}, i = 3, 5, 7, \dots. \tag{36}$$

Here, subscript 'v' denotes average velocity on plate. 'p' denotes sound pressure (average pressure on a hemispherical surface 1 m from the plate center); 'i' denotes superharmonic order. (e.g., $T_{v,3}$ = energy pumping transfer index for the 3rd vibration harmonic).

The ratio T represents energy pumping from fundamental to superharmonic. Besides, $S_{vp,i}$ measures the amplification from vibration superharmonics to transmitted sound superharmonics due to geometrical nonlinearity. Moreover, the following relationships exist between these indicators from Eq. (27) to Eq. (37):

$$p_i \propto \omega_i \cdot \dot{w}_i \Rightarrow S_{vp,i} = \frac{T_{p,i}}{T_{v,i}} = \frac{p_i/p_1}{\dot{w}_i/\dot{w}_1} = \frac{(i \cdot \omega \cdot \dot{w}_i)/(\omega \cdot \dot{w}_1)}{\dot{w}_i/\dot{w}_1} = i; \quad i = 3, 5, 7, \dots. \tag{37}$$

Fig. 10 presents the averaged time-domain vibration waveform and corresponding FFT spectrum at $f_0 = 15$ Hz (within non-resonance band

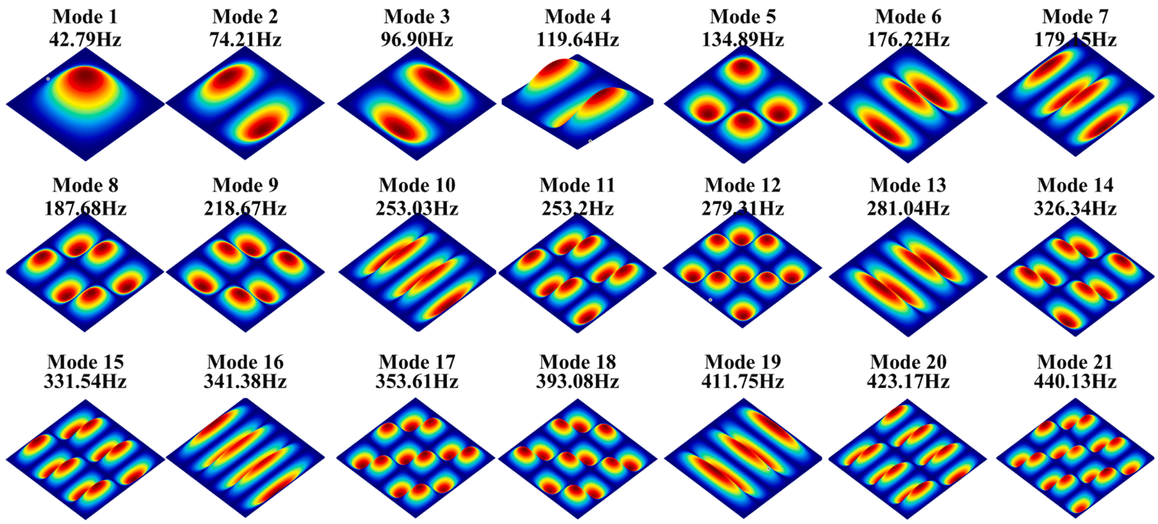

Fig. 7. The linear modes and frequency for the clamp plate modelling by SC-IHB method.

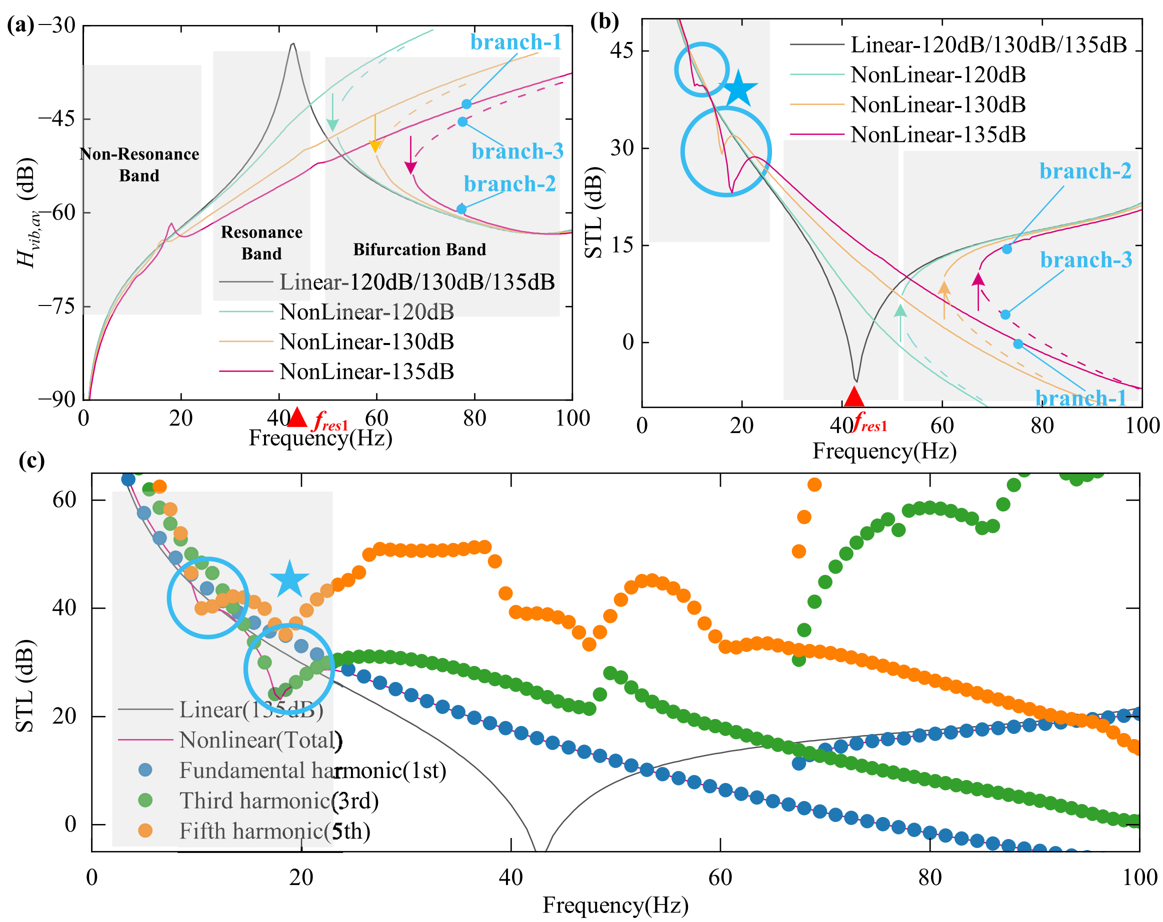

Fig. 8. Bifurcation of the clamp plate under various incident sound pressures with frequency band near f_{res1}. (a) Average vibration transmission $H_{vib,av}$; (b) Sound transmission loss STL; (c) Fundamental and superharmonic component of STL under 135 dB incident sound.

in Fig. 8) under incident pressure of 140 dB. As shown in Fig. 10(a), geometric nonlinearity slightly reduces the total harmonic vibration velocity (0.0746 m/s for linear while 0.0612 m/s for nonlinear), which is consistent with the analytical bifurcation analysis. The velocities of the 3rd (45 Hz) and 5th (75 Hz) harmonics can be extracted from the FFT spectra in Fig. 10(a), yielding $T_{v,3} = 0.602$ and $T_{v,5} = 0.126$. Moreover, the relation of $f_{res1} \approx 3f_0$ and efficient energy transmission in 3rd harmonic indicate the prominent superharmonic resonance condition. The nonlinear phase trajectory in Fig. 11 shows local distortion and self-intersection phenomena, which significantly differ from the linear results.

Though the velocity is slightly reduced by nonlinearity, the total sound amplitude in time domain is greatly improved, nearly doubled due to the superharmonic resonance condition, as shown in Fig. 10(a. b).

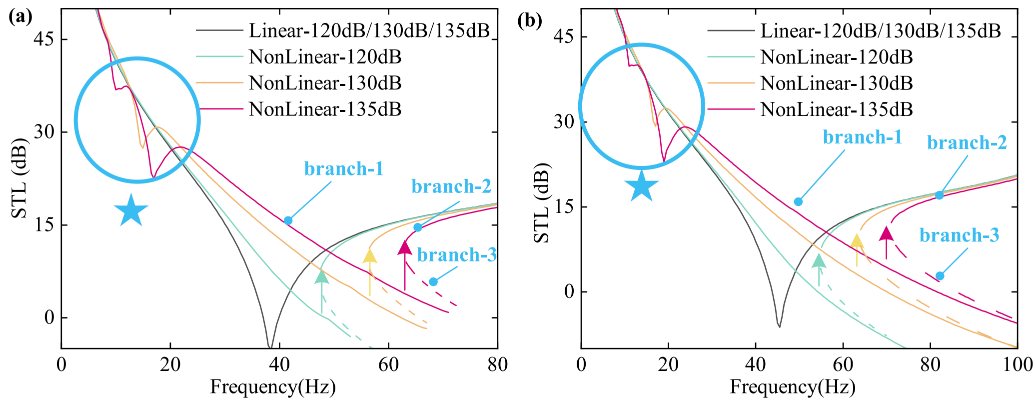

Fig. 9. STL bifurcation of the clamp plate under various stacking sequence. (a) [30°/−30°/30°/−30°]; (b) [0°/90°/0°/90°]. Branch−1 and branch−2 denote the stable solution while branch−3 is unstable.

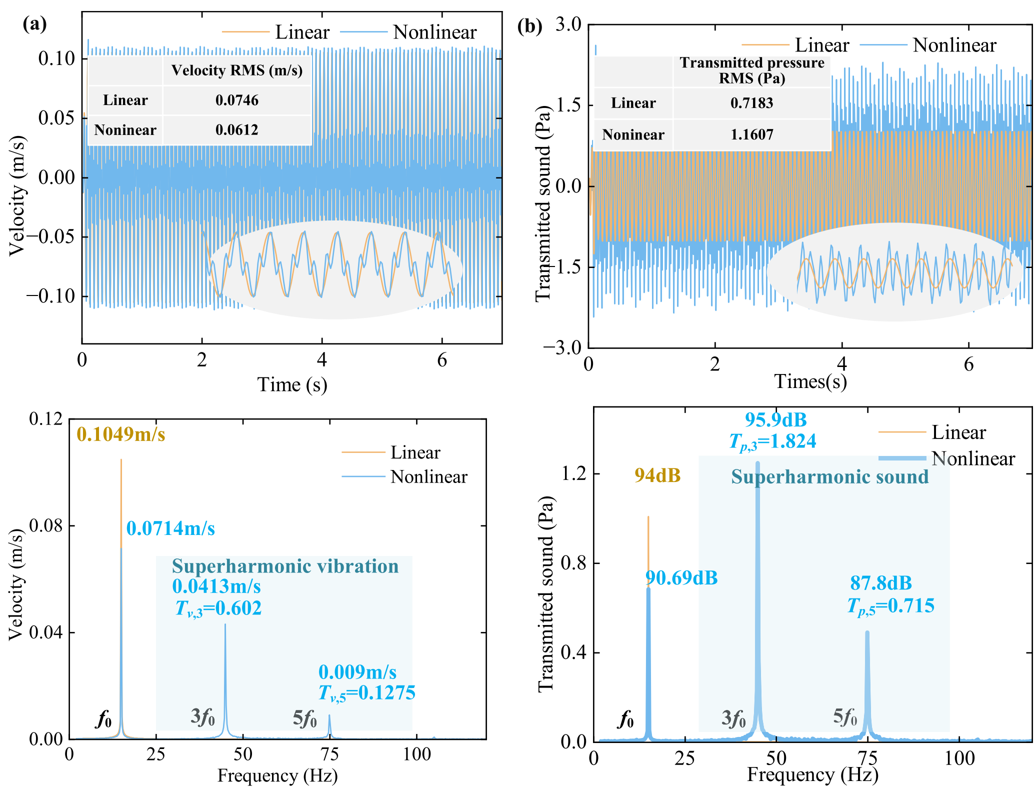

Fig. 10. Time-domain integral results for the clamp plate with incident frequency $f_0 = 15$ Hz within non-resonance band. (a) nonlinear vibration; (b) nonlinear transmitted sound.

Actually, the fundamental component at 15 Hz is reduced by 30% from 1 Pa to 0.7 Pa. However, the transmitted superharmonic sound p_3 and p_5 reaches 1.2 Pa and 0.5 Pa, respectively. The 3rd harmonic even exceeds the fundamental harmonic by 5 dB. The $T_{p,3} = 1.824$ and $T_{p,5} = 0.715$ indicate that the 3rd and 5th harmonics are 182.4% and 71.5% of the fundamental harmonic components, respectively. Obviously, geometric nonlinearity significantly enhances the superharmonic components from velocity to transmitted sound (i.e., $T_{p,3} > T_{v,3}$ and $T_{p,5} > T_{v,5}$). Analyzing the relationships between them, we obtain that $S_{vp,3} = 3.03 \approx 3$ for 3rd harmonic and $S_{vp,5} \approx 5.6$ for 5th harmonic, confirming that the enhancement index S_{vp} is closely equals to the harmonic order. This can be quantitatively demonstrated by the simplified Eq. (27) to Eq. (37): $S_{vp,i} \approx i$ ($i = 3, 5, 7, \ldots$).

The time-domain results for $f_0 = 40$ Hz (within resonance band in Fig. 8) under 140 dB incident sound are shown in Fig. 12. There is only one branch (no bifurcation) of periodic solution as shown in Fig. 8. We obtain $T_{v,3} = 0.169$ and $T_{p,3} = 0.5023$, indicating that the 3rd harmonics for velocity and transmitted sound are 16.9% and 50.23% of the fundamental harmonic, respectively. Therefore, the large deformation plate retains $f_0 \approx f_{res1}$ primary resonance condition. We also have $S_{vp,3} = T_{p,3}/T_{v,3} = 2.97 \approx 3$, confirming the persistent effects of the vibration-to-sound superharmonic enhancement mechanism in the resonance band. Therefore, the total transmitted sound is reduced by 10 dB, as predicted by the bifurcation analyses in Fig. 8: STL at 40 Hz is significantly increased by geometrical nonlinearity.

In addition, as shown in Fig. 6 and Fig. 7, 1st and 4th nature frequency ω_1 and ω_4 (42.79 Hz and 119.64 Hz) satisfy ω_1: ω_4 = 1:3, suggesting the possibility of 1:3 internal resonance. As shown in Fig. 13, we perform the time-domain integration and its FFT results near those two modal frequencies, $f_0 = 40$ Hz and $f_0 = 120$ Hz. The similar superharmonics can be identified

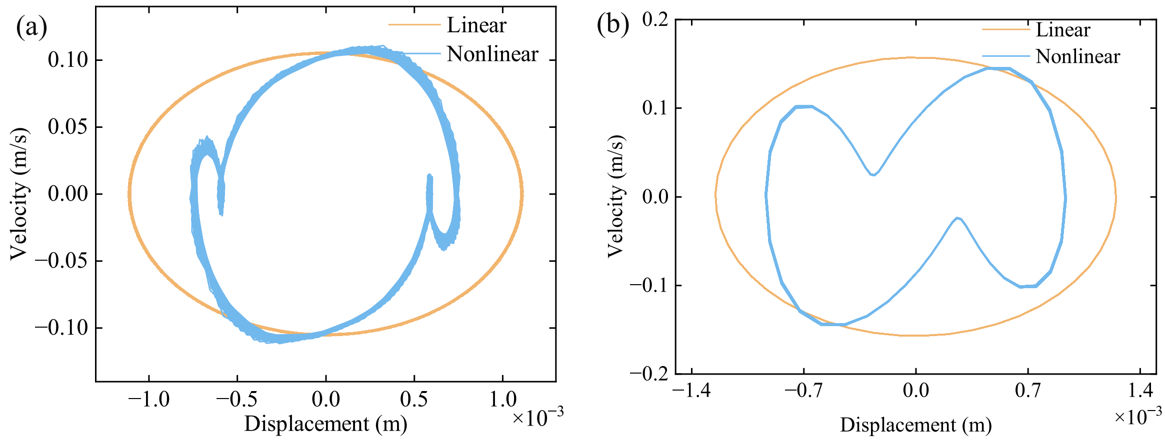

Fig. 11. Phase diagram for the clamp plate with incident sound P_{inci}= 140 dB. (a) f_0 = 15 Hz; (b) f_0 = 20 Hz.

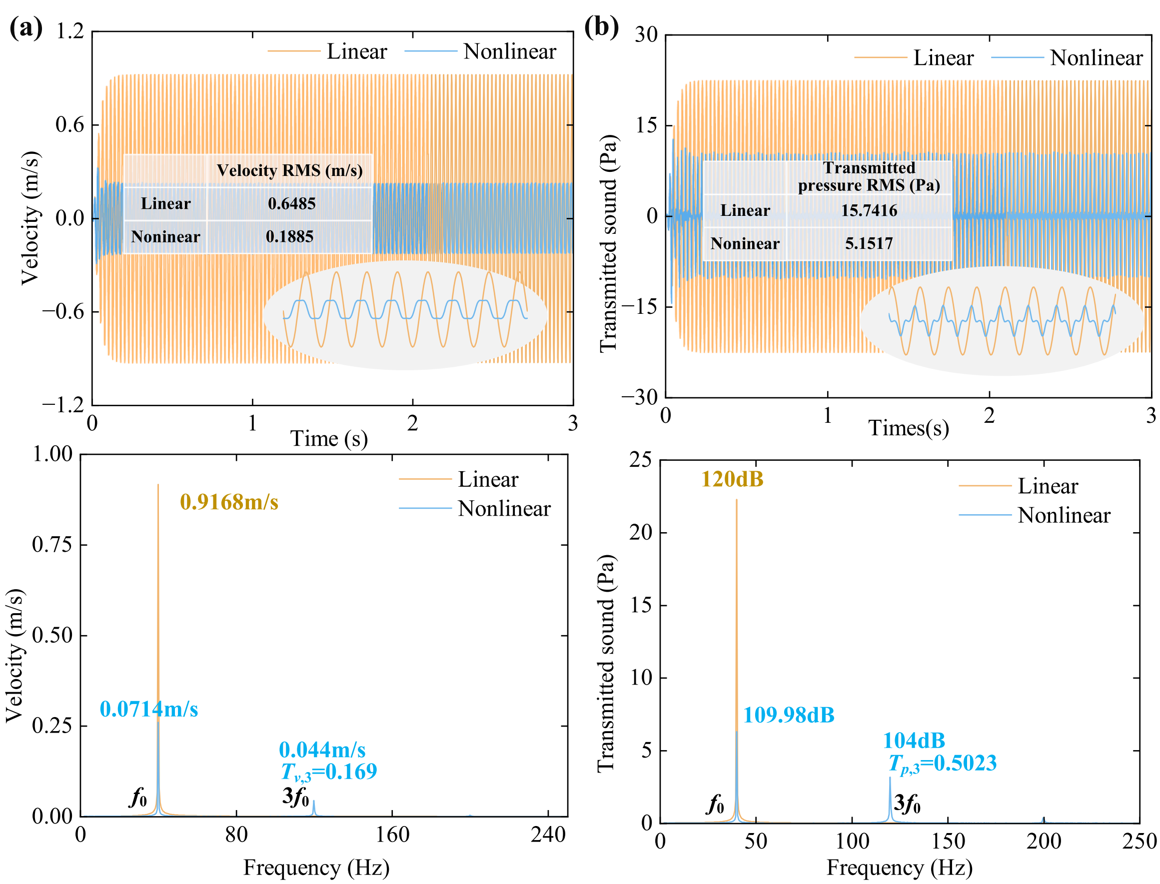

Fig. 12. Time-domain integral results for the clamp plate incident frequency f_0 = 40 Hz within resonance band. (a) nonlinear vibration; (b) nonlinear transmitted sound.

both in f_0 = 40 Hz and 120 Hz. The system response is dominated by primary resonance when f_0 = 40 Hz approaches 1st natural frequency. Although 3th harmonic $3f_0$ = 120 Hz coincide with 4th nature frequency ω_4, no modal energy exchange phenomenon is observed. Similarly, we do not observe any evident energy transfer from the 4th modal frequency to the 1st modal frequency when f_0 = 120 Hz. Therefore, the observed behavior does not correspond to 1:3 internal resonance, but governed by primary resonance and superharmonic generation.

We further investigate the time-domain integral results at f_0 = 70 Hz, within bifurcation band in Fig. 8 under 135 dB. From Fig. 14, it can be observed that geometric nonlinearity slightly enhances the plate vibration and increase the transmitted sound, finally reducing STL, which is consistent with bifurcation results in Fig. 8. Additionally, this observed slight increase in vibration and decrease in STL confirm that the bifurcation solution branch in Fig. 8 jumps from branch−1 to branch−2. We obtain $T_{v,3}$ = 0.0017 and $T_{p,3}$ = 0.0047, indicating the negligible superharmonics.

3.3. Mechanism for superharmonic enhancement

To clarify the mechanism for superharmonic enhancement, this

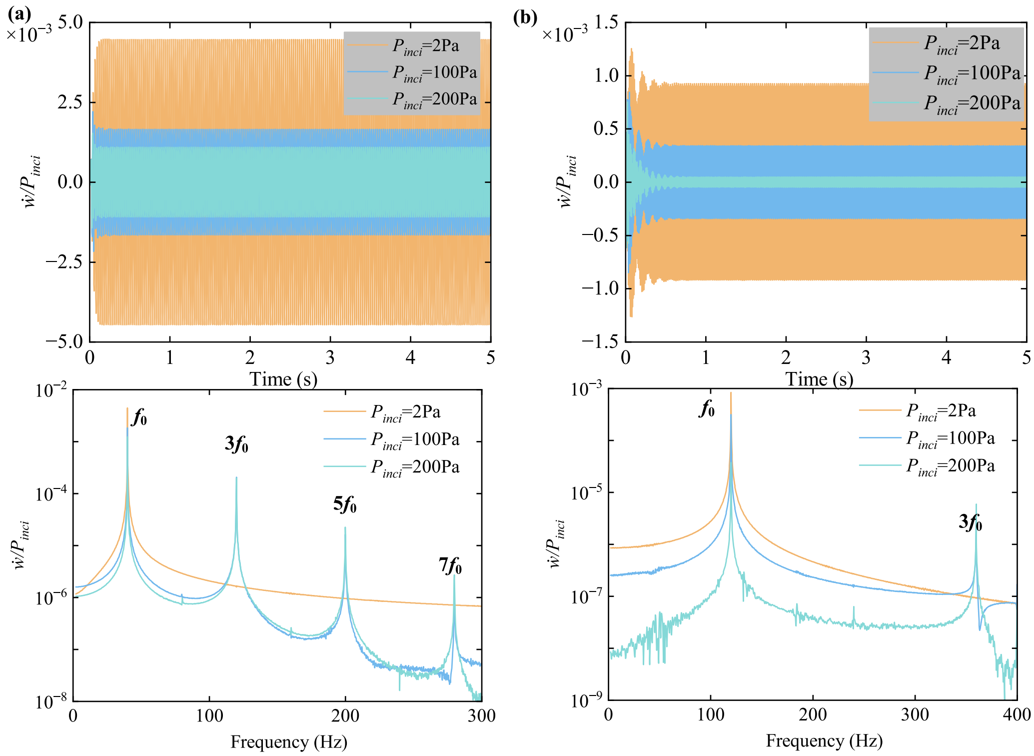

Fig. 13. Time-domain and its FFT results for average velocity under various incident pressure P_{inci}. (a) excitation frequency $f_0 = 40$ Hz. (b) excitation frequency $f_0 = 120$ Hz.

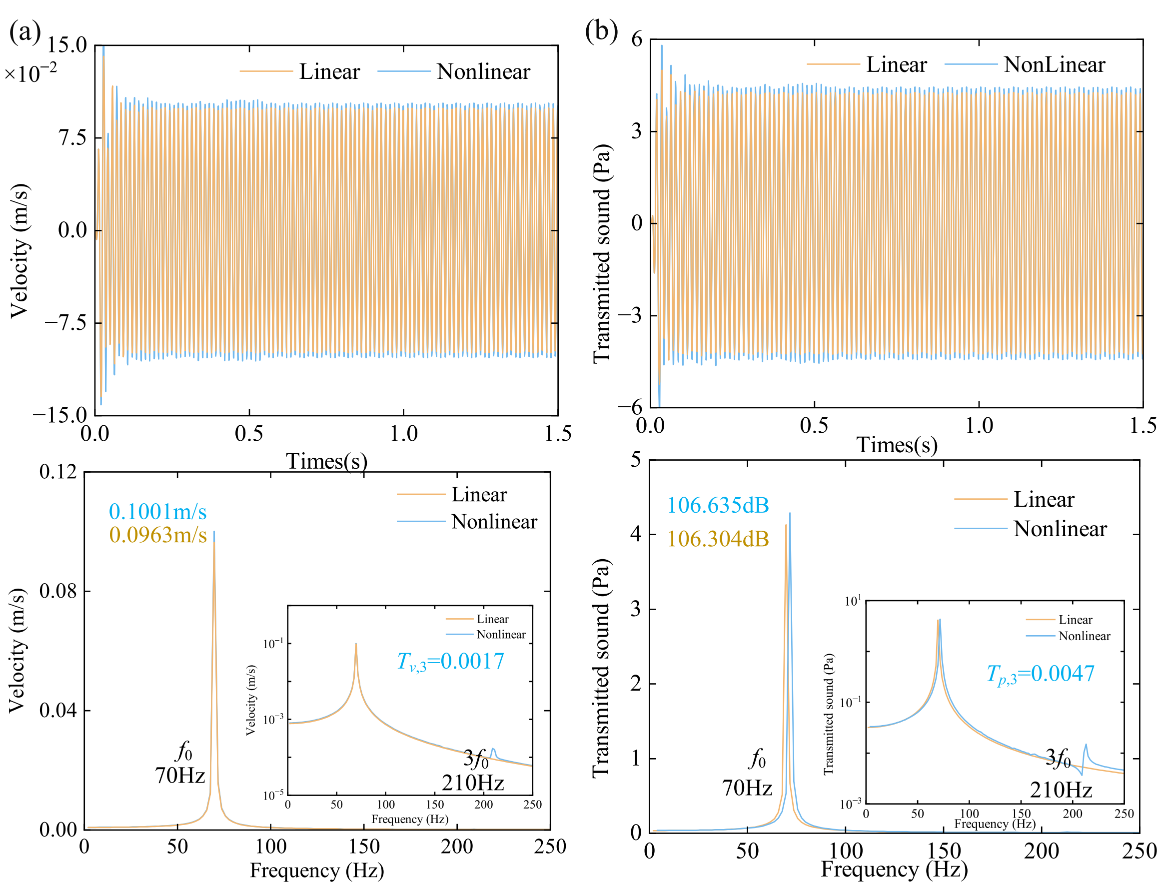

Fig. 14. Time-domain integral results for the clamp plate incident frequency $f_0 = 70$ Hz within bifurcation band. (a) nonlinear vibration; (b) nonlinear transmitted sound.

subsection analyzes the variation trends of the transmitted sound pressure P_{tran} and transmission efficiency P_{tran}/P_{inci} with the incident sound amplitude P_{inci} based on the SC-IHB method. This is like the bifurcation analyses for varying amplitude. Here we pick two frequencies 15 Hz and 20 Hz as examples, which are around the valley in Fig. 8(c) and exhibit superharmonic resonance in Fig. 10. As illustrated in Fig. 15, there is only one branch (no bifurcation) of periodic solution for each incident frequency due to their remoteness to the resonant frequency.

As shown in Fig. 15(a), the fundamental harmonic for P_{tran} and P_{tran}/P_{inci} is continuously decreased relative to the linear result. At low incident amplitudes (<130 dB), superharmonics are significantly smaller than the fundamental wave and nonlinearity slightly suppresses the transmitted sound. As the incident amplitude increases, the total P_{tran} and total P_{tran}/P_{inci} protrude two 'bumps', corresponding to high amplitude and non-negligible 3rd and 5th harmonics. From harmonic components in Fig. 15(a), we know that 'Bump−1′ is primarily caused by 3rd harmonic, and 'Bump−2′ at higher amplitude is induced by 5th harmonic. In addition, the total nonlinear transmission efficiency P_{tran}/P_{inci} is significantly improved, resulting in the reduced sound insulation in Fig. 8(b,c).

As illustrated in Fig. 15(b), the overall pattern for P_{tran} and P_{tran}/P_{inci} at 15 Hz is really similar to that at 20 Hz, except for the difference in the critical point. The threshold for triggering nonlinear effect at 15 Hz is only 130 dB (lower than 135 dB for 20 Hz), owing to the closeness of the 3rd harmonic ($3f_0$ =45 Hz) to the 1st resonance frequency (43 Hz).

3.4. Superharmonic sound radiation mode shape

Based on the SC-IHB method, this subsection can examine the acoustic radiation modes in large deformation plate based on the linear modes displayed in Fig. 7. We note that the 2nd and 3rd modes are antisymmetrical, thus are not excited by the incident plane wave. The 1st and 4th modal modes are excited.

In Fig. 16(a) for f_0 = 15 Hz, the fundamental, 3rd, 5th, and 7th superharmonic acoustic radiation modes are dominated by the 1st linear mode due to superharmonic resonance. The 9th harmonic ($9f_0$ =135 Hz) acoustic radiation mode is approximately dominated by the 4th modal mode. In Fig. 16(b) for f_0 = 20 Hz, 7th harmonic ($7f_0$ = 140 Hz) acoustic radiation mode is approximately the 4th modal mode. In Fig. 16(c) for f_0 = 51 Hz $\approx f_{res1}$, radiation mode for the fundamental harmonic is provided by 1st mode while 3rd harmonic radiation mode is provided by 4th frequency mode. In addition, the 5th and 7th harmonics are provided by more complex nonlinear frequency modes. These results demonstrate that the sound radiation of a harmonic is dominated by the excited vibration mode near the corresponding harmonic.

Moreover, nonlinear frequency mode depends on vibration amplitudes. As shown in Fig. 17, we employ the SC-IHB method to investigate superharmonic acoustic radiation mode excited by different incident sounds. Low incident sound (110 dB) can hardly trigger nonlinearities. Therefore, the acoustic radiation mode for the fundamental harmonic is consistent with the 1st linear frequency mode while for 3rd harmonic is consistent with 4th linear frequency mode. As incident sound level increases, the acoustic radiation mode of fundamental harmonic remains unchanged while those of superharmonics begin to exhibit the fusion of modal peaks. Observing numbers and position of superharmonic mode

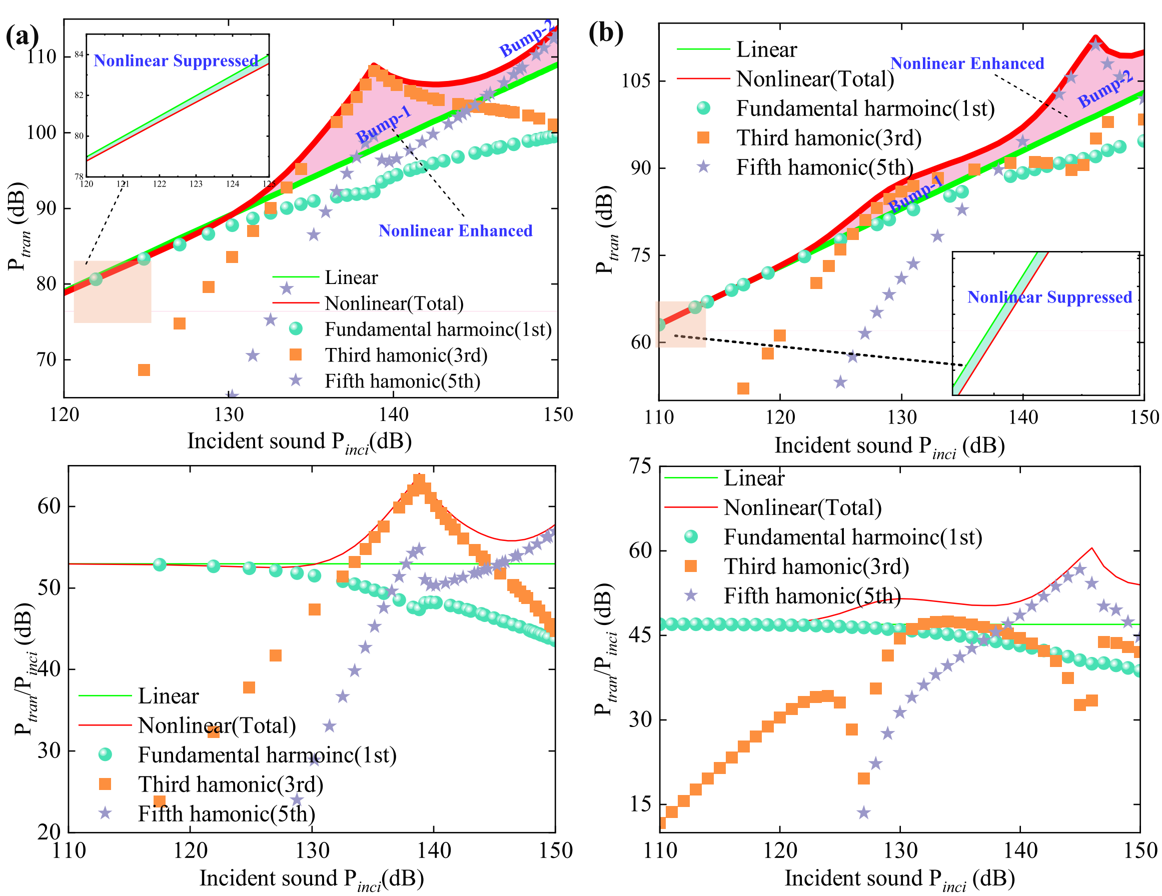

Fig. 15. Transmitted sound P_{tran} and transmission efficiency P_{tran}/P_{inci} with different incident sound pressure levels. (a) excitation frequency f_0 = 20 Hz; (b) Average excitation frequency f_0 = 15 Hz. The green/red solid line represents linear/nonlinear transmitted sound pressure. The green dot, orange square, and grey pentagram represent the fundamental, 3rd, and 5th harmonics.

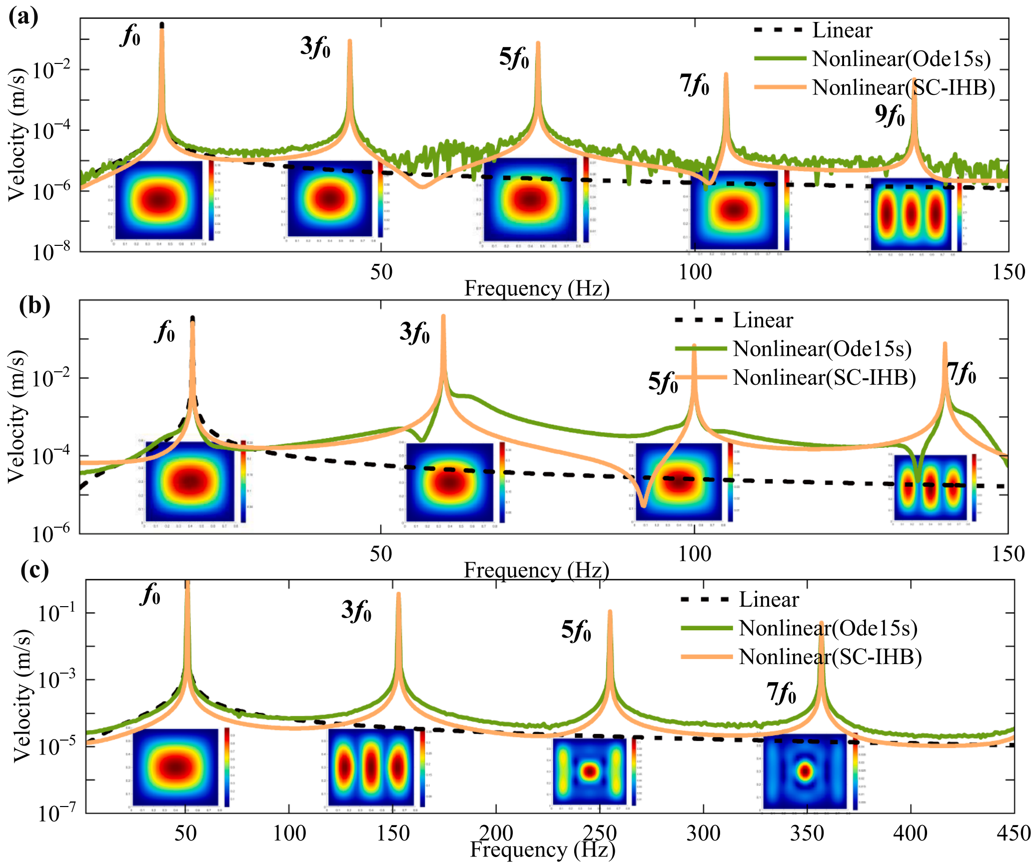

Fig. 16. Fundamental and superharmonic acoustic radiation modes of large deformation plate with various incident frequency f_0. (a) $f_0 = 15$ Hz; (b) $f_0 = 20$ Hz; (c) $f_0 = 51$ Hz.

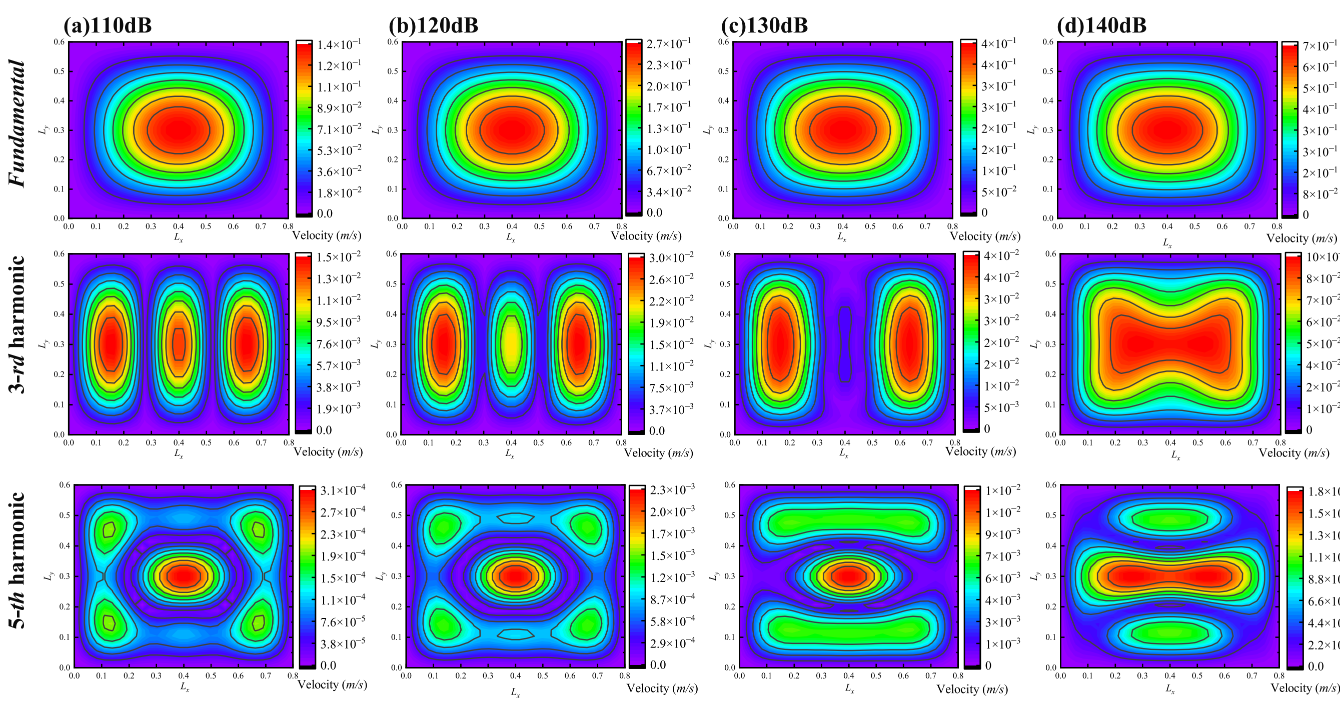

Fig. 17. Acoustic radiation mode diagram of superharmonic under various incident sound pressure. (a) 110 dB; (b) 120 dB; (c) 130 dB; (d) 140 dB.

peaks, and based on radiation cancellation principle[65], the super-harmonic sound radiation efficiency is increasing.

4. Conclusions

This paper addresses the nonlinear vibration and sound transmission of large deformation plates under strong acoustic excitation. A nonlinear amplitude-frequency analysis method is proposed that integrates the Spectral Chebyshev (SC) method with the Incremental Harmonic Balance (IHB) method. Additionally, the geometric nonlinear effect on nonlinear vibration and sound transmission characteristics is elucidated. The main conclusions are summarized as follows:

1) A computational model based on the SC-IHB method is established to balance the high-precision and efficiency of the computational requirement, overcoming the traditional time-domain integration method intensively computing the nonlinear response.
2) The influence of geometrical nonlinear on sound transmission characteristics is elucidated. Within resonance band ($f_0 \approx f_{res1}$), nonlinearity typically suppresses the vibration and significantly increases the STL, due to its primary resonance condition. In non-resonant band, two specific STL valleys are observed at $f_0 \approx 1/3\ f_{res1}$ and $f_0 \approx 1/5\ f_{res1}$. Those area exhibits a new and different physical phenomenon: while nonlinear suppressing the vibration, transmitted sound field is enhanced, thereby compromising the STL. Harmonic component analysis shows that those specific valleys are attributable to superharmonic resonance condition. Furthermore, geometrical nonlinearity reduces the STL in the bifurcation band.
3) The SC-IHB method allows for the understanding of the impact of incident sound pressure level on the transmitted sound pressure (P_{tran}) and transmission efficiency (P_{tran}/P_{inci}). In contrast to the linear system, nonlinearity typically generates 'two bumps' regions of nonlinear enhancement, which are caused by super-harmonic resonance. By analyzing the acoustic radiation mode, we know that the sound radiation of a harmonic is dominated by the excited vibration mode near the corresponding harmonic, and the incident amplitude can change the radiation mode.

CRediT authorship contribution statement

Li Cheng: Writing – review & editing. **Xiansong Gao:** Writing – original draft, Validation, Software, Methodology, Investigation, Conceptualization. **Xin Fang:** Writing – review & editing, Supervision, Methodology, Funding acquisition, Conceptualization.

Funding

This research was funded by the National Natural Science Foundation of China (project numbers 52322505 and 52241103) and the Natural Science Foundation of Hunan Province (project number 2023JJ10055). Hunan Graduate Research Innovation Program (project number XJJCB2026068)

Declaration of Competing Interest

The authors declare that they have no known competing financial interests or personal relationships that could have appeared to influence the work reported in this paper.

Appendix A. Stiffness of fiber composite materials

The appendix main introduces the stiffness of fiber composite material in Eq. (3). According to the Fig. 1(b.2), the elastic stiffness coefficients Q^k writes as:

$$\mathbf{Q}^k = \begin{bmatrix} Q_{11}^k & Q_{12}^k & 0 & 0 & 0 \\ Q_{12}^k & Q_{22}^k & 0 & 0 & 0 \\ 0 & 0 & Q_{44}^k & 0 & 0 \\ 0 & 0 & 0 & Q_{55}^k & 0 \\ 0 & 0 & 0 & 0 & Q_{66}^k \end{bmatrix} = \mathbf{T}_k^T \tilde{\mathbf{Q}}^k \mathbf{T}_k = \mathbf{T}_k^T \begin{bmatrix} \tilde{Q}_{11}^k & \tilde{Q}_{12}^k & 0 & 0 & 0 \\ \tilde{Q}_{12}^k & \tilde{Q}_{22}^k & 0 & 0 & 0 \\ 0 & 0 & \tilde{Q}_{44}^k & 0 & 0 \\ 0 & 0 & 0 & \tilde{Q}_{55}^k & 0 \\ 0 & 0 & 0 & 0 & \tilde{Q}_{66}^k \end{bmatrix} \mathbf{T}_k.$$

Here,$\tilde{Q}^k$ and $\mathbf{T}_k$ denote elastic stiffness coefficients, the material properties of the orthotropic layer and composite transformation matrix.

$$\mathbf{T}_k = \begin{bmatrix} \cos^2\theta_{ply} & \sin^2\theta_{ply} & 0 & 0 & -2\sin\theta_{ply}\cos\theta_{ply} \\ \sin^2\theta_{ply} & \cos^2\theta_{ply} & 0 & 0 & 2\sin\theta_{ply}\cos\theta_{ply} \\ 0 & 0 & \cos\theta_{ply} & \sin\theta_{ply} & 0 \\ 0 & 0 & -\sin\theta_{ply} & \cos\theta_{ply} & 0 \\ \sin\theta_{ply}\cos\theta_{ply} & -\sin\theta_{ply}\cos\theta_{ply} & 0 & 0 & \cos^2\theta_{ply} - \sin^2\theta_{ply} \end{bmatrix}.$$

$$\tilde{Q}_{11}^k = \frac{E_1^k}{1-\mu_{12}^k\mu_{21}^k}; \quad \tilde{Q}_{12}^k = \frac{\mu_{21}^k E_1^k}{1-\mu_{12}^k\mu_{21}^k}; \quad \tilde{Q}_{22}^k = \frac{E_2^k}{1-\mu_{12}^k\mu_{21}^k};$$

$$\tilde{Q}_{44}^k = G_{23}^k; \quad \tilde{Q}_{55}^k = G_{13}^k; \quad \tilde{Q}_{66}^k = G_{12}^k; \quad \frac{\mu_{12}^k}{E_1^k} = \frac{\mu_{21}^k}{E_2^k}.$$

Here, E_1 and E_2 symbol the elastic module of the unidirectional fiber-reinfored material in x and y directions shown in Fig. 1(b.2). μ_{12} denotes the main Poisson's ratio in Fig. 1(b.2).

$$A_{ij} = \sum_{k=1}^{N_{ply}} \widehat{Q}_{ij}^k (z_{k+1} - z_k); \quad B_{ij} = \frac{1}{2}\sum_{k=1}^{N_{ply}} \widehat{Q}_{ij}^k (z_{k+1}^2 - z_k^2); \quad D_{ij} = \frac{1}{3}\sum_{k=1}^{N_{ply}} \widehat{Q}_{ij}^k (z_{k+1}^3 - z_k^3).$$

Here, A, B, D denote the stiffness coefficients.

Appendix B. Detailed system dynamic matrix

The appendix main introduces the displacement solutions in Eq. (10) and detailed dynamic matrix in Eq. (12).

$$\begin{cases} u(x,y) = \sum_{m=0}^{\infty}\sum_{n=0}^{\infty}\Gamma_{mn}(x,y)A_{mn}(t) \cong \mathbf{\Gamma}_A(x,y)\mathbf{A}(t) = [\mathbf{\Gamma}_M(x)\otimes\mathbf{\Gamma}_N(y)]\mathbf{A}(t) \\ v(x,y) = \sum_{m=0}^{\infty}\sum_{n=0}^{\infty}\Gamma_{mn}(x,y)B_{mn}(t) \cong \mathbf{\Gamma}_B(x,y)\mathbf{B}(t) = [\mathbf{\Gamma}_M(x)\otimes\mathbf{\Gamma}_N(y)]\mathbf{B}(t) \\ w(x,y) = \sum_{m=0}^{\infty}\sum_{n=0}^{\infty}\Gamma_{mn}(x,y)C_{mn}(t) \cong \mathbf{\Gamma}_C(x,y)\mathbf{C}(t) = [\mathbf{\Gamma}_M(x)\otimes\mathbf{\Gamma}_N(y)]\mathbf{C}(t) \\ \phi_x(x,y) = \sum_{m=0}^{\infty}\sum_{n=0}^{\infty}\Gamma_{mn}(x,y)D_{mn}(t) \cong \mathbf{\Gamma}_D(x,y)\mathbf{D}(t) = [\mathbf{\Gamma}_M(x)\otimes\mathbf{\Gamma}_N(y)]\mathbf{D}(t) \\ \phi_y(x,y) = \sum_{m=0}^{\infty}\sum_{n=0}^{\infty}\Gamma_{mn}(x,y)E_{mn}(t) \cong \mathbf{\Gamma}_E(x,y)\mathbf{E}(t) = [\mathbf{\Gamma}_M(x)\otimes\mathbf{\Gamma}_N(y)]\mathbf{E}(t) \end{cases}.$$

Where $\otimes$ indicates Kronecker product. $(M+1)$ and $(N+1)$ represent the truncation numbers of the Chebyshev polynomials selected in the x and y directions, respectively.

$$\begin{cases} \mathbf{\Gamma}_M(x) = [\Gamma_0(x),\ldots,\Gamma_m(x),\ldots,\Gamma_M(x)] \\ \mathbf{\Gamma}_N(y) = [\Gamma_0(y),\ldots,\Gamma_n(y),\ldots,\Gamma_N(y)] \\ \Gamma_0(x) = 1, \Gamma_1(x) = x, \Gamma_m(x) = 2x\Gamma_{m-1}(x) - \Gamma_{m-2}(x), m\geq 2 \\ \Gamma_0(y) = 1, \Gamma_1(y) = y, \Gamma_n(y) = 2y\Gamma_{n-1}(y) - \Gamma_{n-2}(y), n\geq 2 \end{cases}.$$

$$\begin{cases} \mathbf{A}(t) = [A_{00},\ldots,A_{0N},\ldots,A_{m0},\ldots,A_{mN},\ldots,A_{M0}\ldots,A_{MN}]^T \\ \mathbf{B}(t) = [B_{00},\ldots,B_{0N},\ldots,B_{m0},\ldots,B_{mN},\ldots,B_{M0}\ldots,B_{MN}]^T \\ \mathbf{C}(t) = [C_{00},\ldots,C_{0N},\ldots,C_{m0},\ldots,C_{mN},\ldots,C_{M0}\ldots,C_{MN}]^T \\ \mathbf{D}(t) = [D_{00},\ldots,D_{0N},\ldots,D_{m0},\ldots,D_{mN},\ldots,D_{M0}\ldots,D_{MN}]^T \\ \mathbf{E}(t) = [E_{00},\ldots,E_{0N},\ldots,E_{m0},\ldots,E_{mN},\ldots,E_{M0}\ldots,E_{MN}]^T \end{cases}.$$

$$\mathbf{M}\ddot{\mathbf{q}}(t) + \mathbf{C}\dot{\mathbf{q}}(t) + [\mathbf{K}_\mathbf{L} + \mathbf{K}_\mathbf{NL}(\mathbf{q}(t))]\mathbf{q}(t) = \mathbf{F}\cos\omega t$$

The matrix of the elastic plate is represented in detail below:

$$\mathbf{F} = \int_0^{L_y}\int_0^{L_x}\left[\mathbf{\Gamma}^T p(x,y,t)\right]\mathrm{d}x\mathrm{d}y,$$

$$\mathbf{C} = \alpha_c\mathbf{M} + \beta_c\mathbf{K},$$

here, α_c and β_c are the Rayleigh damping coefficients, $\alpha_c = 0$ and $\beta_c = 1e{-}5$. In addition, this paper also considers sound radiation damping, with reference to Norton et al.[66].

$$\mathbf{K}_\mathbf{L} = \begin{bmatrix} \mathbf{K}_{11} & \mathbf{K}_{12} & \mathbf{0} & \mathbf{K}_{14} & \mathbf{K}_{15} \\ \mathbf{K}_{12}^\mathrm{T} & \mathbf{K}_{22} & \mathbf{0} & \mathbf{K}_{24} & \mathbf{K}_{25} \\ \mathbf{0} & \mathbf{0} & \mathbf{K}_{33} & \mathbf{K}_{34} & \mathbf{K}_{35} \\ \mathbf{K}_{14}^\mathrm{T} & \mathbf{K}_{24}^\mathrm{T} & \mathbf{K}_{34}^\mathrm{T} & \mathbf{K}_{44} & \mathbf{K}_{45} \\ \mathbf{K}_{15}^\mathrm{T} & \mathbf{K}_{25}^\mathrm{T} & \mathbf{K}_{35}^\mathrm{T} & \mathbf{K}_{45}^\mathrm{T} & \mathbf{K}_{55} \end{bmatrix}.$$

The subscripts ‘,x’ and ‘,y’ denote the partial derivatives of the Chebyshev polynomial vector function $\mathbf{\Gamma}$ with respect to x and y, respectively.

$$\mathbf{K}_{11} = \int_0^{L_y}\int_0^{L_x}\left[A_{11}\mathbf{\Gamma}_{,x}^T\mathbf{\Gamma}_{,x} + A_{66}\mathbf{\Gamma}_{,y}^T\mathbf{\Gamma}_{,y} + A_{16}\mathbf{\Gamma}_{,y}^T\mathbf{\Gamma}_{,x} + A_{16}\mathbf{\Gamma}_{,x}^T\mathbf{\Gamma}_{,y}\right]\mathrm{d}x\mathrm{d}y$$
$$+\int_0^{L_x}\left(k_{uy0}\mathbf{\Gamma}^T\mathbf{\Gamma}|_{y=0} + k_{uyL_2}\mathbf{\Gamma}^T\mathbf{\Gamma}|_{y=L_y}\right)\mathrm{d}x + \int_0^{L_y}\left(k_{ux0}\mathbf{\Gamma}^T\mathbf{\Gamma}|_{x=0} + k_{uxL_1}\mathbf{\Gamma}^T\mathbf{\Gamma}|_{x=L_x}\right)\mathrm{d}y.$$

$$\mathbf{K}_{12} = \int_0^{L_y}\int_0^{L_x}\left[A_{12}\mathbf{\Gamma}_{,x}^T\mathbf{\Gamma}_{,y} + A_{66}\mathbf{\Gamma}_{,y}^T\mathbf{\Gamma}_{,x} + A_{16}\mathbf{\Gamma}_{,x}^T\mathbf{\Gamma}_{,x} + A_{26}\mathbf{\Gamma}_{,y}^T\mathbf{\Gamma}_{,y}\right]\mathrm{d}x\mathrm{d}y.$$

$$\mathbf{K}_{14} = \int_0^{L_y}\int_0^{L_x}\left[B_{11}\mathbf{\Gamma}_{,x}^T\mathbf{\Gamma}_{,x} + B_{66}\mathbf{\Gamma}_{,y}^T\mathbf{\Gamma}_{,y} + B_{16}\mathbf{\Gamma}_{,y}^T\mathbf{\Gamma}_{,x} + B_{16}\mathbf{\Gamma}_{,x}^T\mathbf{\Gamma}_{,y}\right]\mathrm{d}x\mathrm{d}y.$$

$$\mathbf{K}_{15}=\int_0^{L_y}\int_0^{L_x}\left[B_{12}\boldsymbol{\Gamma}_{,x}^T\boldsymbol{\Gamma}_{,y}+B_{66}\boldsymbol{\Gamma}_{,y}^T\boldsymbol{\Gamma}_{,x}+B_{16}\boldsymbol{\Gamma}_{,x}^T\boldsymbol{\Gamma}_{,x}+B_{26}\boldsymbol{\Gamma}_{,y}^T\boldsymbol{\Gamma}_{,y}\right]\mathrm{d}x\mathrm{d}y.$$

$$\mathbf{K}_{22}=\int_0^{L_y}\int_0^{L_x}\left[A_{22}\boldsymbol{\Gamma}_{,y}^T\boldsymbol{\Gamma}_{,y}+A_{66}\boldsymbol{\Gamma}_{,x}^T\boldsymbol{\Gamma}_{,x}+A_{26}\boldsymbol{\Gamma}_{,x}^T\boldsymbol{\Gamma}_{,y}+A_{26}\boldsymbol{\Gamma}_{,y}^T\boldsymbol{\Gamma}_{,x}\right]\mathrm{d}x\mathrm{d}y$$
$$+\int_0^{L_x}\left(k_{vy0}\boldsymbol{\Gamma}^T\boldsymbol{\Gamma}\big|_{y=0}+k_{vyL_2}\boldsymbol{\Gamma}^T\boldsymbol{\Gamma}\big|_{y=L_y}\right)\mathrm{d}x+\int_0^{L_y}\left(k_{vx0}\boldsymbol{\Gamma}^T\boldsymbol{\Gamma}|_{x=0}+k_{vxL_1}\boldsymbol{\Gamma}^T\boldsymbol{\Gamma}|_{x=L_x}\right)\mathrm{d}y.$$

$$\mathbf{K}_{24}=\int_0^{L_y}\int_0^{L_x}\left[\mathbf{B}_{12}\boldsymbol{\Gamma}_{,y}^T\boldsymbol{\Gamma}_{,x}+B_{66}\boldsymbol{\Gamma}_{,x}^T\boldsymbol{\Gamma}_{,y}+B_{16}\boldsymbol{\Gamma}_{,x}^T\boldsymbol{\Gamma}_{,x}+B_{26}\boldsymbol{\Gamma}_{,y}^T\boldsymbol{\Gamma}_{,y}\right]\mathrm{d}x\mathrm{d}y.$$

$$\mathbf{K}_{25}=\int_0^{L_y}\int_0^{L_x}\left[B_{22}\boldsymbol{\Gamma}_{,y}^T\boldsymbol{\Gamma}_{,y}+B_{66}\boldsymbol{\Gamma}_{,x}^T\boldsymbol{\Gamma}_{,x}+B_{26}\boldsymbol{\Gamma}_{,x}^T\boldsymbol{\Gamma}_{,y}+B_{26}\boldsymbol{\Gamma}_{,y}^T\boldsymbol{\Gamma}_{,x}\right]\mathrm{d}x\mathrm{d}y.$$

$$\mathbf{K}_{33}=\kappa_s\int_0^{L_y}\int_0^{L_x}\left[A_{44}\boldsymbol{\Gamma}_{,y}^T\boldsymbol{\Gamma}_{,y}+A_{55}\boldsymbol{\Gamma}_{,x}^T\boldsymbol{\Gamma}_{,x}+A_{45}\boldsymbol{\Gamma}_{,x}^T\boldsymbol{\Gamma}_{,y}+A_{45}\boldsymbol{\Gamma}_{,y}^T\boldsymbol{\Gamma}_{,x}\right]\mathrm{d}x\mathrm{d}y$$
$$+\int_0^{L_x}\left(k_{wy0}\boldsymbol{\Gamma}^\mathrm{T}\boldsymbol{\Gamma}\big|_{y=0}+k_{wyL_2}\boldsymbol{\Gamma}^\mathrm{T}\boldsymbol{\Gamma}\big|_{y=L_y}\right)\mathrm{d}x+\int_0^{L_y}\left(k_{wx0}\boldsymbol{\Gamma}^\mathrm{T}\boldsymbol{\Gamma}|_{x=0}+k_{wxL_1}\boldsymbol{\Gamma}^\mathrm{T}\boldsymbol{\Gamma}|_{x=L_x}\right)\mathrm{d}y.$$

$$\mathbf{K}_{34}=\kappa_s\int_0^{L_y}\int_0^{L_x}\left[A_{55}\boldsymbol{\Gamma}_{,x}^T\boldsymbol{\Gamma}+A_{45}\boldsymbol{\Gamma}_{,y}^T\boldsymbol{\Gamma}\right]\mathrm{d}x\mathrm{d}y.$$

$$\mathbf{K}_{35}=\kappa_s\int_0^{L_y}\int_0^{L_x}\left[A_{44}\boldsymbol{\Gamma}_{,y}^T\boldsymbol{\Gamma}+A_{45}\boldsymbol{\Gamma}_{,x}^T\boldsymbol{\Gamma}\right]\mathrm{d}x\mathrm{d}y.$$

$$\mathbf{K}_{44}=\int_0^{L_y}\int_0^{L_x}\left[\kappa_sA_{55}\boldsymbol{\Gamma}^T\boldsymbol{\Gamma}+D_{11}\boldsymbol{\Gamma}_{,x}^T\boldsymbol{\Gamma}_{,x}+D_{66}\boldsymbol{\Gamma}_{,y}^T\boldsymbol{\Gamma}_{,y}+D_{16}\boldsymbol{\Gamma}_{,x}^T\boldsymbol{\Gamma}_{,y}+D_{16}\boldsymbol{\Gamma}_{,y}^T\boldsymbol{\Gamma}_{,x}\right]\mathrm{d}x\mathrm{d}y$$
$$+\int_0^{L_x}\left(k_{xy0}\boldsymbol{\Gamma}^T\boldsymbol{\Gamma}\big|_{y=0}+k_{xyL_2}\boldsymbol{\Gamma}^T\boldsymbol{\Gamma}\big|_{y=L_y}\right)\mathrm{d}x+\int_0^{L_y}\left(k_{xx0}\boldsymbol{\Gamma}^T\boldsymbol{\Gamma}|_{x=0}+k_{xxL_1}\boldsymbol{\Gamma}^T\boldsymbol{\Gamma}|_{x=L_x}\right)\mathrm{d}y.$$

$$\mathbf{K}_{45}=\int_0^{L_y}\int_0^{L_x}\left[\kappa_sA_{45}\boldsymbol{\Gamma}^T\boldsymbol{\Gamma}+D_{12}\boldsymbol{\Gamma}_{,x}^T\boldsymbol{\Gamma}_{,y}+D_{66}\boldsymbol{\Gamma}_{,y}^T\boldsymbol{\Gamma}_{,x}+D_{16}\boldsymbol{\Gamma}_{,x}^T\boldsymbol{\Gamma}_{,x}+D_{26}\boldsymbol{\Gamma}_{,y}^T\boldsymbol{\Gamma}_{,y}\right]\mathrm{d}x\mathrm{d}y.$$

$$\mathbf{K}_{55}=\int_0^{L_y}\int_0^{L_x}\left[\kappa_sA_{44}\boldsymbol{\Gamma}^T\boldsymbol{\Gamma}+D_{22}\boldsymbol{\Gamma}_{,y}^T\boldsymbol{\Gamma}_{,y}+D_{66}\boldsymbol{\Gamma}_{,x}^T\boldsymbol{\Gamma}_{,x}+D_{26}\boldsymbol{\Gamma}_{,x}^T\boldsymbol{\Gamma}_{,y}+D_{26}\boldsymbol{\Gamma}_{,y}^T\boldsymbol{\Gamma}_{,x}\right]\mathrm{d}x\mathrm{d}y$$
$$+\int_0^{L_x}\left(k_{yy0}\boldsymbol{\Gamma}^T\boldsymbol{\Gamma}\big|_{y=0}+k_{yyL_2}\boldsymbol{\Gamma}^T\boldsymbol{\Gamma}\big|_{y=L_y}\right)\mathrm{d}x+\int_0^{L_y}\left(k_{yx0}\boldsymbol{\Gamma}^T\boldsymbol{\Gamma}|_{x=0}+k_{yxL_1}\boldsymbol{\Gamma}^T\boldsymbol{\Gamma}|_{x=L_x}\right)\mathrm{d}y.$$

$$\mathbf{M}=\begin{bmatrix}\mathbf{M}_{11}&\mathbf{0}&\mathbf{0}&\mathbf{M}_{14}&\mathbf{0}\\\mathbf{0}&\mathbf{M}_{22}&\mathbf{0}&\mathbf{0}&\mathbf{M}_{25}\\\mathbf{0}&\mathbf{0}&\mathbf{M}_{33}&\mathbf{0}&\mathbf{0}\\\mathbf{M}_{14}^\mathrm{T}&\mathbf{0}&\mathbf{0}&\mathbf{M}_{44}&\mathbf{0}\\\mathbf{0}&\mathbf{M}_{25}^\mathrm{T}&\mathbf{0}&\mathbf{0}&\mathbf{M}_{55}\end{bmatrix}.$$

$$\mathbf{M}_{11}=\int_0^{L_y}\int_0^{L_x}I_0\boldsymbol{\Gamma}^T\boldsymbol{\Gamma}\mathrm{d}x\mathrm{d}y;\quad\mathbf{M}_{14}=\int_0^{L_y}\int_0^{L_x}I_1\boldsymbol{\Gamma}^T\boldsymbol{\Gamma}\mathrm{d}x\mathrm{d}y;\quad\mathbf{M}_{22}=\int_0^{L_y}\int_0^{L_x}I_0\boldsymbol{\Gamma}^T\boldsymbol{\Gamma}\mathrm{d}x\mathrm{d}y;\quad\mathbf{M}_{25}=\int_0^{L_y}\int_0^{L_x}I_1\boldsymbol{\Gamma}^T\boldsymbol{\Gamma}\mathrm{d}x\mathrm{d}y;$$
$$\mathbf{M}_{33}=\int_0^{L_y}\int_0^{L_x}I_0\boldsymbol{\Gamma}^T\boldsymbol{\Gamma}\mathrm{d}x\mathrm{d}y;\quad\mathbf{M}_{44}=\int_0^{L_y}\int_0^{L_x}I_2\boldsymbol{\Gamma}^T\boldsymbol{\Gamma}\mathrm{d}x\mathrm{d}y;\quad\mathbf{M}_{55}=\int_0^{L_y}\int_0^{L_x}I_2\boldsymbol{\Gamma}^T\boldsymbol{\Gamma}\mathrm{d}x\mathrm{d}y.$$

$$\mathbf{K}_{\mathbf{NL}}=\begin{bmatrix}\mathbf{0}&\mathbf{0}&\mathbf{K}_{\mathbf{NL},13}&\mathbf{0}&\mathbf{0}\\\mathbf{0}&\mathbf{0}&\mathbf{K}_{\mathbf{NL},23}&\mathbf{0}&\mathbf{0}\\\mathbf{K}_{\mathbf{NL},31}&\mathbf{K}_{\mathbf{NL},32}&\mathbf{K}_{\mathbf{NL},33}&\mathbf{K}_{\mathbf{NL},34}&\mathbf{K}_{\mathbf{NL},35}\\\mathbf{0}&\mathbf{0}&\mathbf{K}_{\mathbf{NL},43}&\mathbf{0}&\mathbf{0}\\\mathbf{0}&\mathbf{0}&\mathbf{K}_{\mathbf{NL},53}&\mathbf{0}&\mathbf{0}\end{bmatrix}.$$

$$\mathbf{K}_{\mathbf{NL},13}=\frac{1}{2}\int_0^{L_y}\int_0^{L_x}\left(A_{11}\boldsymbol{\Gamma}_{,x}^TC^T\boldsymbol{\Gamma}_{,x}^T\boldsymbol{\Gamma}_{,x}+A_{12}\boldsymbol{\Gamma}_{,x}^TC^T\boldsymbol{\Gamma}_{,y}^T\boldsymbol{\Gamma}_{,y}+2A_{66}\boldsymbol{\Gamma}_{,y}^TC^T\boldsymbol{\Gamma}_{,x}^T\boldsymbol{\Gamma}_{,y}\right)\mathrm{d}x\mathrm{d}y.$$

$$\mathbf{K}_{\mathbf{NL},23}=\frac{1}{2}\int_0^{L_y}\int_0^{L_x}\left(A_{12}\boldsymbol{\Gamma}_{,y}^TC^T\boldsymbol{\Gamma}_{,x}^T\boldsymbol{\Gamma}_{,x}+A_{22}\boldsymbol{\Gamma}_{,y}^TC^T\boldsymbol{\Gamma}_{,y}^T\boldsymbol{\Gamma}_{,y}+2A_{66}\boldsymbol{\Gamma}_{,x}^TC^T\boldsymbol{\Gamma}_{,x}^T\boldsymbol{\Gamma}_{,y}\right)\mathrm{d}x\mathrm{d}y.$$

$$\mathbf{K}_{\mathbf{NL},31}=\frac{1}{2}\int_0^{L_y}\int_0^{L_x}\left(2A_{11}\boldsymbol{\Gamma}_{,x}^TC^T\boldsymbol{\Gamma}_{,x}^T\boldsymbol{\Gamma}_{,x}+2A_{12}\boldsymbol{\Gamma}_{,x}^TC^T\boldsymbol{\Gamma}_{,y}^T\boldsymbol{\Gamma}_{,y}+2A_{66}\boldsymbol{\Gamma}_{,y}^TC^T\boldsymbol{\Gamma}_{,x}^T\boldsymbol{\Gamma}_{,y}+2A_{66}\boldsymbol{\Gamma}_{,y}^TC^T\boldsymbol{\Gamma}_{,y}^T\boldsymbol{\Gamma}_{,x}\right)\mathrm{d}x\mathrm{d}y.$$

$$\mathbf{K}_{\mathbf{NL},32} = \frac{1}{2}\int_0^{L_y}\int_0^{L_x}\left(+2A_{12}\boldsymbol{\Gamma}_{,y}^T C^T \boldsymbol{\Gamma}_{,x}^T \boldsymbol{\Gamma}_{,x} + 2A_{22}\boldsymbol{\Gamma}_{,y}^T C^T \boldsymbol{\Gamma}_{,y}^T \boldsymbol{\Gamma}_{,y} + 2A_{66}\boldsymbol{\Gamma}_{,x}^T C^T \boldsymbol{\Gamma}_{,x}^T \boldsymbol{\Gamma}_{,y} + 2A_{66}\boldsymbol{\Gamma}_{,x}^T C^T \boldsymbol{\Gamma}_{,y}^T \boldsymbol{\Gamma}_{,x}\right)\mathrm{d}x\mathrm{d}y.$$

$$\mathbf{K}_{\mathbf{NL},33} = \frac{1}{2}\int_0^{L_y}\int_0^{L_x}\begin{pmatrix} A_{11}\boldsymbol{\Gamma}_{,x}^T C^T \boldsymbol{\Gamma}_{,x}^T \boldsymbol{\Gamma}_{,x} C\boldsymbol{\Gamma}_{,x} + A_{12}\boldsymbol{\Gamma}_{,x}^T C^T \boldsymbol{\Gamma}_{,x}^T \boldsymbol{\Gamma}_{,y} C\boldsymbol{\Gamma}_{,y} + A_{12}\boldsymbol{\Gamma}_{,y}^T C^T \boldsymbol{\Gamma}_{,y}^T \boldsymbol{\Gamma}_{,x} C\boldsymbol{\Gamma}_{,x} \\ +A_{22}\boldsymbol{\Gamma}_{,y}^T C^T \boldsymbol{\Gamma}_{,y}^T \boldsymbol{\Gamma}_{,y} C\boldsymbol{\Gamma}_{,y} + 2A_{66}\boldsymbol{\Gamma}_{,x}^T C^T \boldsymbol{\Gamma}_{,x}^T \boldsymbol{\Gamma}_{,y} C\boldsymbol{\Gamma}_{,y} + 2A_{66}\boldsymbol{\Gamma}_{,y}^T C^T \boldsymbol{\Gamma}_{,y}^T \boldsymbol{\Gamma}_{,x} C\boldsymbol{\Gamma}_{,x} \end{pmatrix}\mathrm{d}x\mathrm{d}y.$$

$$\mathbf{K}_{\mathbf{NL},34} = \frac{1}{2}\int_0^{L_y}\int_0^{L_x}\left(2B_{11}\boldsymbol{\Gamma}_{,x}^T C^T \boldsymbol{\Gamma}_{,x}^T \boldsymbol{\Gamma}_{,x} + 2B_{12}\boldsymbol{\Gamma}_{,x}^T C^T \boldsymbol{\Gamma}_{,y}^T \boldsymbol{\Gamma}_{,y} + 2B_{66}\boldsymbol{\Gamma}_{,y}^T C^T \boldsymbol{\Gamma}_{,x}^T \boldsymbol{\Gamma}_{,y} + 2B_{66}\boldsymbol{\Gamma}_{,y}^T C^T \boldsymbol{\Gamma}_{,y}^T \boldsymbol{\Gamma}_{,x}\right)\mathrm{d}x\mathrm{d}y.$$

$$\mathbf{K}_{\mathbf{NL},35} = \frac{1}{2}\int_0^{L_y}\int_0^{L_x}\left(2B_{12}\boldsymbol{\Gamma}_{,y}^T C^T \boldsymbol{\Gamma}_{,x}^T \boldsymbol{\Gamma}_{,x} + 2B_{22}\boldsymbol{\Gamma}_{,y}^T C^T \boldsymbol{\Gamma}_{,y}^T \boldsymbol{\Gamma}_{,y} + 2B_{66}\boldsymbol{\Gamma}_{,x}^T C^T \boldsymbol{\Gamma}_{,x}^T \boldsymbol{\Gamma}_{,y} + 2B_{66}\boldsymbol{\Gamma}_{,x}^T C^T \boldsymbol{\Gamma}_{,y}^T \boldsymbol{\Gamma}_{,x}\right)\mathrm{d}x\mathrm{d}y.$$

$$\mathbf{K}_{\mathbf{NL},43} = \frac{1}{2}\int_0^{L_y}\int_0^{L_x}\left(B_{11}\boldsymbol{\Gamma}_{,x}^T C^T \boldsymbol{\Gamma}_{,x}^T \boldsymbol{\Gamma}_{,x} + B_{12}\boldsymbol{\Gamma}_{,x}^T C^T \boldsymbol{\Gamma}_{,y}^T \boldsymbol{\Gamma}_{,y} + 2B_{66}\boldsymbol{\Gamma}_{,y}^T C^T \boldsymbol{\Gamma}_{,x}^T \boldsymbol{\Gamma}_{,y}\right)\mathrm{d}x\mathrm{d}y.$$

$$\mathbf{K}_{\mathbf{NL},53} = \frac{1}{2}\int_0^{L_y}\int_0^{L_x}\left(B_{12}\boldsymbol{\Gamma}_{,y}^T C^T \boldsymbol{\Gamma}_{,x}^T \boldsymbol{\Gamma}_{,x} + B_{22}\boldsymbol{\Gamma}_{,y}^T C^T \boldsymbol{\Gamma}_{,y}^T \boldsymbol{\Gamma}_{,y} + 2B_{66}\boldsymbol{\Gamma}_{,x}^T C^T \boldsymbol{\Gamma}_{,x}^T \boldsymbol{\Gamma}_{,y}\right)\mathrm{d}x\mathrm{d}y.$$

Appendix C. Detailed Matrix of IHB method

This appendix details the IHB method for nonlinear solutions in Eq. (19)(20).

$$\boldsymbol{\zeta}_0 = \left[\zeta_{1,0}, \zeta_{2,0}, \ldots, \zeta_{j,0}, \ldots, \zeta_{100,0}\right]^T; \quad \Delta\boldsymbol{\zeta}_0 = \left[\Delta\zeta_1, \Delta\zeta_2, \ldots, \Delta\zeta_j, \ldots, \Delta\zeta_{100}\right]^T$$
$$\mathbf{f}_0 = \left[f_{1,0}, f_{2,0}, \ldots, f_{j,0}, \ldots, f_{100,0}\right]^T; \quad \Delta\mathbf{f} = \left[\Delta f_1, \Delta f_2, \ldots, \Delta f_j, \ldots, \Delta f_{100}\right]^T.$$

$$\begin{cases} \mathbf{C}_s = [1 \quad \cos\tau \quad \cos 2\tau \quad \cdots \quad \cos N_h\tau \quad \sin\tau \quad \sin 2\tau \quad \cdots \quad \sin N_h\tau] \\ \mathbf{A}_j = \left[a_{j,0} \quad a_{j,1} \quad a_{j,2} \quad \cdots \quad a_{j,N_h} \quad b_{j,1} \quad b_{j,2} \quad \cdots \quad b_{j,N_h}\right]^T \\ \Delta\mathbf{A}_j = \left[\Delta a_{j,0} \quad \Delta a_{j,1} \quad \Delta a_{j,2} \quad \cdots \quad \Delta a_{j,N_h} \quad \Delta b_{j,1} \quad \Delta b_{j,2} \quad \cdots \quad \Delta b_{j,N_h}\right]^T \end{cases}$$

Superharmonic expansions can be obtained for all matrix elements similar to Eq. (20) rewritten as

$$\boldsymbol{\zeta}_0 = \mathbf{SA}, \Delta\boldsymbol{\zeta} = \mathbf{S}\Delta\mathbf{A}.$$

$$\mathbf{A} = [\mathbf{A}_1, \mathbf{A}_2, \ldots, \mathbf{A}_{100}]; \quad \Delta\mathbf{A} = [\Delta\mathbf{A}_1, \Delta\mathbf{A}_2, \ldots, \Delta\mathbf{A}_{100}]; \quad \mathbf{S} = diag[\mathbf{C}_s, \mathbf{C}_s, \ldots, \mathbf{C}_s].$$

the algebraic equations for solving Eq. (19) can be written as

$$\mathbf{K}_{mc}\Delta\mathbf{A} = \mathbf{R} - \mathbf{R}_{mc}\Delta\omega + \mathbf{R}_f\Delta\mathbf{f},$$

$$\begin{cases} \mathbf{K}_{mc} = \displaystyle\int_0^{2\pi}\mathbf{S}^T\left[\omega_0^2\mathbf{m}\ddot{\mathbf{S}} + \omega_0\mathbf{c}\dot{\mathbf{S}} + \left(\mathbf{k} + \frac{\partial\mathbf{k}_{nl}\boldsymbol{\zeta}_0}{\partial\boldsymbol{\zeta}_0}\right)\mathbf{S}\right]\mathrm{d}\tau \\ \mathbf{R} = \displaystyle\int_0^{2\pi}\mathbf{S}^T\left\{\mathbf{f}\cos(\tau) - \left[\omega_0^2\mathbf{m}\ddot{\mathbf{S}} + \omega_0\mathbf{c}\dot{\mathbf{S}} + (\mathbf{k} + \mathbf{k}_{nl})\mathbf{S}\right]\mathbf{A}\right\}\mathrm{d}\tau \\ \mathbf{R}_{mc} = \displaystyle\int_0^{2\pi}\mathbf{S}^T\left(2\omega_0\mathbf{m}\ddot{\mathbf{S}} + \mathbf{c}\dot{\mathbf{S}}\right)\mathbf{A}\mathrm{d}\tau \end{cases}.$$

To more clear represent the formation of the matrix and facilitate programming, the matrix can be rewritten as:

$$\begin{cases} \mathbf{K}_{mc} = \omega_0^2\overline{\mathbf{m}} + \omega_0\overline{\mathbf{c}} + \overline{\mathbf{k}} + \overline{\mathbf{k}}_{nl}^{(1)} \\ \mathbf{R}_{mc} = (2\omega_0\overline{\mathbf{m}} + \overline{\mathbf{c}})\mathbf{A} \\ \mathbf{R} = \overline{\mathbf{f}} - \left[\omega_0^2\mathbf{m} + \omega_0\overline{\mathbf{c}} + (\overline{\mathbf{k}} + \overline{\mathbf{k}}_{nl})\right]\mathbf{A} \end{cases},$$

here,

$$\overline{\mathbf{m}} = \int_0^{2\pi}\mathbf{S}^T\omega_0^2\mathbf{m}\ddot{\mathbf{S}}\mathrm{d}\tau; \quad \overline{\mathbf{c}} = \int_0^{2\pi}\mathbf{S}^T\omega_0\mathbf{c}\dot{\mathbf{S}}\mathrm{d}\tau; \quad \overline{\mathbf{k}} = \int_0^{2\pi}\mathbf{S}^T\mathbf{k}\mathbf{S}\mathrm{d}\tau;$$
$$\overline{\mathbf{k}}_{nl}^{(1)} = \int_0^{2\pi}\mathbf{S}^T\frac{\partial\mathbf{k}_{nl}\boldsymbol{\zeta}_0}{\partial\boldsymbol{\zeta}_0}\mathbf{S}\mathrm{d}\tau; \quad \overline{\mathbf{f}} = \int_0^{2\pi}\mathbf{S}^T\mathbf{f}\cos(\tau)\mathbf{S}\mathrm{d}\tau.$$

Data Availability

Data will be made available on request.

References

[1] R.-B. Hao, Z.-Q. Lu, H. Ding, L.-Q. Chen, A nonlinear vibration isolator supported on a flexible plate: analysis and experiment, Nonlinear Dyn. 108 (2022) 941–958.
[2] A. Mitra, P. Sahoo, K. Saha, Nonlinear vibration analysis of simply supported stiffened plate by a variational method, Mech. Adv. Mater. Struct. 20 (2013) 373–396.
[3] T. Ma, W. Zhang, Y. Zhang, A. Amer, Nonlinear vibrations, bifurcations and chaos of piezoelectric composite lattice sandwich plate with four simply supported edges, Chaos Solitons Fractals 183 (2024) 114940.
[4] M.W. Teng, Y.Q. Wang, Nonlinear forced vibration of simply supported functionally graded porous nanocomposite thin plates reinforced with graphene platelets, Thin-Walled Struct. 164 (2021) 107799.
[5] A.J. Lee, D.J. Inman, Electromechanical modelling of a bistable plate with macro fiber composites under nonlinear vibrations, J. Sound. Vib. 446 (2019) 326–342.
[6] X. Guo, W. Zhang, Y. Zhang, Experimental and numerical investigations on nonlinear snap-through vibrations of an asymmetrically composite laminated bistable thin plate simple supported at four corners, Eng. Struct. 296 (2023) 116926.
[7] X. Fang, P. Sheng, J. Wen, W. Chen, L. Cheng, A nonlinear metamaterial plate for suppressing vibration and sound radiation, Int. J. Mech. Sci. 228 (2022) 107473.
[8] X. Fang, J. Wen, B. Bonello, J. Yin, D. Yu, Ultra-low and ultra-broad-band nonlinear acoustic metamaterials, Nat. Commun. 8 (2017) 1288.
[9] C.-s Zhu, X.-q Fang, J.-x Liu, Relationship between nonlinear free vibration behavior and nonlinear forced vibration behavior of viscoelastic plates, Commun. Nonlinear Sci. Numer. Simul. 117 (2023) 106926.
[10] P. Sheng, B. Hu, X. Fang, J. Wen, Random aeroelastic vibration of nonlinear metamaterial supersonic plates, Int. J. Mech. Sci. (2025) 110371.
[11] P. Sheng, X. Fang, L. Dai, D. Yu, J. Wen, Synthetical vibration reduction of the nonlinear acoustic metamaterial honeycomb sandwich plate, Mech. Syst. Signal. Process. 185 (2023) 109774.
[12] W. Wei, F. Guan, X. Fang, A low-frequency and broadband wave-insulating vibration isolator based on plate-shaped metastructures, Appl. Math. Mech. 45 (2024) 1171–1188.
[13] X. Fang, W. Lacarbonara, L. Cheng, Advances in nonlinear acoustic/elastic metamaterials and metastructures, Nonlinear Dyn. (2024) 1–28.
[14] T. Li, X. Fang, J. Wen, Significantly broaden sound insulation of metamaterial plate via strongly nonlinear interaction, Nonlinear Dyn. (2025) 1–16.
[15] S. Soleymani, P. Memarzadeh, D. Toghraie, An enhanced strain gradient model for temperature-dependent sound transmission loss in double-walled functionally graded microplates, Thin-Walled Struct. 201 (2024) 112001.
[16] T. Fu, Z. Chen, H. Yu, Z. Wang, X. Liu, An analytical study of sound transmission through corrugated core FGM sandwich plates filled with porous material, Composites Part B Engineering 151 (2018) 161–172.
[17] X. Fang, J. Wen, L. Cheng, D. Yu, H. Zhang, P. Gumbsch, Programmable gear-based mechanical metamaterials, Nat. Mater. 21 (2022) 869–876.
[18] X. Fang, D. Yu, J. Wen, Y. Dai, M.R. Begley, H. Gao, P. Gumbsch, Large recoverable elastic energy in chiral metamaterials via twist buckling, Nature (2025) 1–7.
[19] J. Zhang, M. Xiao, L. Gao, A. Alù, F. Wang, Self-bridging metamaterials surpassing the theoretical limit of Poisson's ratios, Nat. Commun. 14 (2023) 4041.
[20] K. Wu, J.-J. Liu, Y.-j Ding, W. Wang, B. Liang, J.-C. Cheng, Metamaterial-based real-time communication with high information density by multipath twisting of acoustic wave, Nat. Commun. 13 (2022) 5171.
[21] J. Zhang, S. Zhang, X. Zhou, Y. He, F. Wang, D. Yu, Y. Jiang, M. Xiao, X. Fang, Cut-Enabled Mechanical Metamaterials for Multimodal and Reprogrammable Static Nonreciprocity, Adv. Sci. (2025) e03455.
[22] S. Xu, Y. Wang, L. Liu, F. Zeng, H. Yang, J. Zhong, Z. Zheng, D. Yu, J. Wen, Inverse design of hydroacoustic absorbing metastructures via incorporating multi-material topology optimization into semi-analytical method, Appl. Math. Model. (2025) 116265.
[23] Y. Song, J. Wen, H. Tian, X. Lu, Z. Li, L. Feng, Vibration and sound properties of metamaterial sandwich panels with periodically attached resonators: Simulation and experiment study, J. Sound. Vib. 489 (2020) 115644.
[24] S.A. Cummer, J. Christensen, A. Alù, Controlling sound with acoustic metamaterials, Nat. Rev. Mater. 1 (2016) 1–13.
[25] A. Chen, Y.F. Xia, Z.X. Chen, H.J. Su, J.J. Liu, J. Yang, X.F. Zhu, B. Liang, J. C. Cheng, Dynamic and High-Precision Sound Manipulation by Acoustic Metamaterial-Empowered Phased Arrays, Adv. Funct. Mater. (2025) 2425833.
[26] Y. Li, J. Zhang, J. Li, S. Guo, Design of a broadband composite noise reduction metamaterial with integrated vibration reduction and sound absorption and insulation, Mater. Des. 238 (2024) 112709.
[27] C. Du, Y. Yang, P. Du, Q. Hu, Z. Huang, F. Ma, Broadband sound penetration enhancement on water-air interface by metalens, Thin-Walled Struct. (2025) 113450.
[28] L.C. Cheung, S.K. Lele, Linear and nonlinear processes in two-dimensional mixing layer dynamics and sound radiation, J. Fluid. Mech. 625 (2009) 321–351.
[29] J. Ginsberg, Multi-dimensional non-linear acoustic wave propagation, Part II: The non-linear interaction of an acoustic fluid and plate under harmonic excitation, J. Sound. Vib. 40 (1975) 359–379.
[30] J. Ginsberg, A re-examination of the non-linear interaction between an acoustic fluid and a flat plate undergoing harmonic excitation, J. Sound. Vib. 60 (1978) 449–458.
[31] A. Nayfeh, S.G. Kelly, Non-linear interactions of acoustic fields with plates under harmonic excitations, J. Sound. Vib. 60 (1978) 371–377.
[32] H. Liu, Y. Qu, S. Liu, G. Meng, Nonlinear supersonic flutter of a composite panel backed by an acoustic cavity with finite-amplitude sound waves, Int. J. Mech. Sci. 268 (2024) 109038.
[33] G. Wang, Y. Qu, Y. Li, A hybrid multi-scale/finite element method in arbitrary Lagrangian-Eulerian framework for predicting nonlinear structural-acoustic responses of a large-deformable beam in fluid, J. Sound. Vib. 577 (2024) 118333.
[34] S. Liu, F. Xie, Y. Qu, P. Gao, G. Meng, Fluid-structure-acoustic responses of a nonlinearly supported rigid circular cylinder in viscous flow, Phys. Fluids 37 (2025).
[35] J. Zhu, Y. Qu, H. Gao, G. Meng, Nonlinear sound absorption of Helmholtz resonators with serrated necks under high-amplitude sound wave excitation, J. Sound. Vib. 537 (2022) 117197.
[36] Y. Tang, W. He, F. Xin, T.J. Lu, Nonlinear sound absorption of ultralight hybrid-cored sandwich panels, Mech. Syst. Signal. Process. 135 (2020) 106428.
[37] X. Fang, T. Li, B. Hu, M. Yu, P. Sheng, J. Wen, L. Cheng, Breaking the mass law for broadband sound insulation through strongly nonlinear interactions, New. J. Phys. 25 (2023) 093010.
[38] X. Fang, J. Wen, J. Yin, D. Yu, Highly efficient continuous bistable nonlinear energy sink composed of a cantilever beam with partial constrained layer damping, Nonlinear Dyn. 87 (2017) 2677–2695.
[39] Z. Wang, Y. Xing, G. Li, Closed-form solutions for the free vibrations of three-dimensional orthotropic rectangular plates, Int. J. Mech. Sci. 199 (2021) 106398.
[40] Z. Li, T. Ye, G. Jin, Tj Yang, L. Tian, Y. Chen, A unified dynamic stiffness modeling of multi-plate coupled systems with discrete spring connections, Thin-Walled Struct. 205 (2024).
[41] S. Meng, Q. Wang, R. Zhong, B. Qin, Legendre–Ritz solutions for vibration characteristics of three-dimensional double-layer lattice truss sandwich plates, Thin-Walled Struct. 203 (2024) 112185.
[42] R. Zhong, Q. Wang, S. Hu, B. Qin, C. Shuai, Spectral element modeling and experimental investigations on vibration behaviors of imperfect plate considering irregular hole and curved crack, J. Sound. Vib. 529 (2022) 116924.
[43] X. Gao, Q. Wang, X. Liu, R. Zhong, B. Qin, H. Xu, An electro-mechanical shell model for predicting stochastic vibration behavior of smart piezoelectric structure utilizing the Spectral-Tchebyche method, Eng. Anal. Bound. Elem. 155 (2023) 584–598.
[44] X. Gao, R. Zhong, X. Liu, Q. Wang, H. Xu, Stationary stochastic response behaviors of FG plate–shell combined structure in aero-thermal environment, Int. J. Struct. Stab. Dyn. 24 (2024) 2450164.
[45] X. Gao, R. Zhong, Q. Wang, Q. Bin, H. Xu, Spectral-Tchebychev technique for the free and stochastic vibration analysis of functionally graded plates with piezoelectric patches, Eng. Anal. Bound. Elem. 152 (2023) 688–703.
[46] Y. Wang, Z. Zhang, W. Zhang, Suppression of nonlinear aeroelastic responses of graphene platelet-reinforced composite lattice sandwich plates using a nonlinear energy sink, Nonlinear Dyn. 112 (2024) 12925–12939.
[47] Y. Hu, Y. Tian, Primary parametric resonance, stability analysis and bifurcation characteristics of an axially moving ferromagnetic rectangular thin plate under the action of air-gap field, Nonlinear Dyn. 112 (2024) 8889–8920.
[48] H. Hu, R. Zhong, Q. Wang, J.-a. Duan, Stochastic dynamic analysis and parameter optimization of dynamic vibration absorbers for vibration suppression of combined plate systems, Aerosp. Sci. Technol. 177 (2026) 112937.
[49] Q. Wang, R. Wang, R. Zhong, X. Wu, J.-a. Duan, Nonlinear dynamic of aircraft-like shell coupled with internal nonlinear components, Mech. Syst. Signal Process. 249 (2026) 114049.
[50] R. Zhong, Y. Wang, R. Wang, Q. Wang, J.-a. Duan, Uncertainty vibro-acoustic behaviours of cracked plates using spectral-MRGP method, Int. J. Mech. Sci. 327 (2026) 111949.
[51] H. Abramovich, Stability and vibrations of thin-walled composite structures, Woodhead Publishing,, 2017.
[52] Y. Song, Q. Li, K. Xue, An analytical method for vibration analysis of arbitrarily shaped non-homogeneous orthotropic plates of variable thickness resting on Winkler-Pasternak foundation, Compos. Struct. 296 (2022) 115885.
[53] X. Xie, G. Jin, An efficient domain decomposition approach for the free and forced vibration analysis of plate assemblies, Thin-Walled Struct. 216 (2025) 113621.
[54] Z. Guo, S. Zhao, Y. Zhang, Y. Zhang, J. Yang, Multi-physics field induced buckling and free vibration of annular perovskite plates, Compos. Struct. 354 (2025) 118791.
[55] X. Shi, P. Zuo, R. Zhong, C. Guo, Q. Wang, Vibration analysis of combined functionally graded cylindrical-conical shells coupled with annular plates in thermal environment, Compos. Struct. 294 (2022) 115738.
[56] K. Tian, Y. Wang, B. Fang, D. Cao, K. Yu, X. Mei, A novel unified dynamical modeling of perforated plates based on negative mass equivalence, Mech. Syst. Signal. Process. 232 (2025) 112723.
[57] R. Wang, R. Zhong, Q. Wang, A SGM-IHB approach for nonlinear free and forced vibration analysis of FG-GPLRC beams rested on viscoelastic foundation, Nonlinear Dyn. 113 (2025) 5171–5191.
[58] Z. Wu, Y. Zhang, G. Yao, 3/2 superharmonic resonance and 1/2 subharmonic resonance of functionally graded carbon nanotube reinforced composite beams, Compos. Struct. 241 (2020) 112056.
[59] L.A. Roussos, Noise transmission loss of a rectangular plate in an infinite baffle, in: Meeting, Acoust. Soc. Am. (1985).
[60] N. Chandra, S. Raja, K.N. Gopal, Vibro-acoustic response and sound transmission loss analysis of functionally graded plates, J. Sound. Vib. 333 (2014) 5786–5802.
[61] K. Zhou, Z. Lin, X. Huang, H. Hua, Vibration and sound radiation analysis of temperature-dependent porous functionally graded material plates with general boundary conditions, Appl. Acoust. 154 (2019) 236–250.

[62] Q. Geng, Y. Li, Analysis of dynamic and acoustic radiation characters for a flat plate under thermal environments, Int. J. Appl. Mech. 4 (2012) 1250028.
[63] F. Boumédiène, A. Miloudi, J.-M. Cadou, L. Duigou, E. Boutyour, Nonlinear forced vibration of damped plates by an asymptotic numerical method, Comput. Struct. 87 (2009) 1508–1515.
[64] P. Ribeiro, Nonlinear vibrations of simply-supported plates by the p-version finite element method, Finite Elem. Anal. Des. 41 (2005) 911–924.
[65] F.J. Fahy, Sound and structural vibration: radiation, transmission and response, Elsevier (2007).
[66] M.P. Norton, D.G. Karczub, Fundamentals of noise and vibration analysis for engineers, Cambridge university press,, 2003.